Earth and Planetary Science Letters 375 (2013) 57–70

Contents lists available at ScienceDirect

Earth and Planetary Science Letters

journal homepage: www.elsevier.com/locate/epsl

# The October 28, 2012 $M_w$ 7.8 Haida Gwaii underthrusting earthquake and tsunami: Slip partitioning along the Queen Charlotte Fault transpressional plate boundary

Thorne Lay [a,*], Lingling Ye [a], Hiroo Kanamori [b], Yoshiki Yamazaki [c], Kwok Fai Cheung [c], Kevin Kwong [d], Keith D. Koper [d]

[a] Department of Earth and Planetary Sciences, University of California Santa Cruz, Santa Cruz, CA 95064, USA
[b] Seismological Laboratory, California Institute of Technology, Pasadena, CA 91125, USA
[c] Department of Ocean and Resources Engineering, University of Hawai'i, Honolulu, HI 96822, USA
[d] Department of Geology and Geophysics, University of Utah, Salt Lake City, UT 84112, USA

ARTICLE INFO

*Article history:*
Received 13 March 2013
Received in revised form
26 April 2013
Accepted 1 May 2013
Editor: P. Shearer
Available online 12 June 2013

*Keywords:*
Haida Gwaii earthquake
Queen Charlotte Fault
tsunami

ABSTRACT

The Pacific/North American plate boundary is undergoing predominantly right-lateral strike–slip motion along the Queen Charlotte and Fairweather transform faults. The Queen Charlotte Fault (QCF) hosted the largest historical earthquake in Canada, the 1949 $M_S$ 8.1 strike–slip earthquake, which ruptured from offshore northern Haida Gwaii several hundred kilometers northwestward. On January 5, 2013 an $M_w$ 7.5 strike–slip faulting event occurred near the northern end of the 1949 rupture zone. Along central and southern Haida Gwaii the relative plate motion has ~20% oblique convergence across the left-stepping plate boundary. There had been uncertainty in how the compressional component of plate motion is accommodated. The October 28, 2012 $M_w$ 7.8 Haida Gwaii earthquake involved slightly (~20°) oblique thrust faulting on a shallow (~18.5°) northeast-dipping fault plane with strike (~320°) parallel to the QCF, consistent with prior inferences of Pacific Plate underthrusting beneath Haida Gwaii. The rupture extended to shallow depth offshore of Moresby Island beneath a 25–30 km wide terrace of sediments that has accumulated in a wedge seaward of the QCF. The shallow thrusting caused seafloor uplift that generated substantial localized tsunami run-up and a modest far-field tsunami that spread across the northern Pacific, prompting a tsunami warning, beach closure, and coastal evacuation in Hawaii, although ultimately tide gauges showed less than 0.8 m of water level increase. The mainshock rupture appears to have spread with a ~2.3 km/s rupture velocity over a length of ~150 km, with slip averaging 3.3 m concentrated beneath the sedimentary wedge. The event was followed by a substantial aftershock sequence, in which almost all of the larger events involve distributed intraplate normal faulting extending ~50 km oceanward from the QCF. The highly oblique slip partitioning in southern Haida Gwaii is distinctive in that the local plate boundary-parallel motion on the QCF may be accommodated either by infrequent large strike–slip ruptures or by aseismic creep, as seems to be the case for deeper oblique relative plate motion beneath Haida Gwaii, while the sedimentary terrace accumulates plate boundary-perpendicular compressional strain that releases in almost pure thrust faulting earthquakes, seaward of the QCF.



## 1. Introduction

Restraining bends along strike–slip faults are usually accompanied by localized folding and uplift, as well as oblique or partitioned thrust and strike–slip faulting, with two notable examples along the San Andreas fault being located near the Transverse Ranges and the Santa Cruz Mountains. The plate boundary between the northeastern Pacific plate and the North American plate extending from British Columbia to the Alaskan subduction zone is primarily a right-lateral strike–slip transform fault boundary along the Fairweather Fault (FF) and Queen Charlotte Fault (QCF). There is a gradual left-stepping bend in the southern portion of the QCF (Fig. 1) extending from the Winona Block/Explorer Plate to along Moresby Island, the southern large island of Haida Gwaii (formerly Queen Charlotte Islands). Plate motions are close to boundary-parallel along the FF and QCF north of Haida Gwaii, and purely right-lateral strike–slip faulting is commonly observed for the larger events, exemplified by the January 5, 2013 ($M_w$ 7.5) Craig, Alaska event shown in Fig. 1a, and the earlier July 10,

* Corresponding author. Tel.: +1 831459 3164; fax: +1 831459 3074.
*E-mail address:* tlay@ucsc.edu (T. Lay).

0012-821X/$ - see front matter © 2013 Elsevier B.V. All rights reserved.
http://dx.doi.org/10.1016/j.epsl.2013.05.005

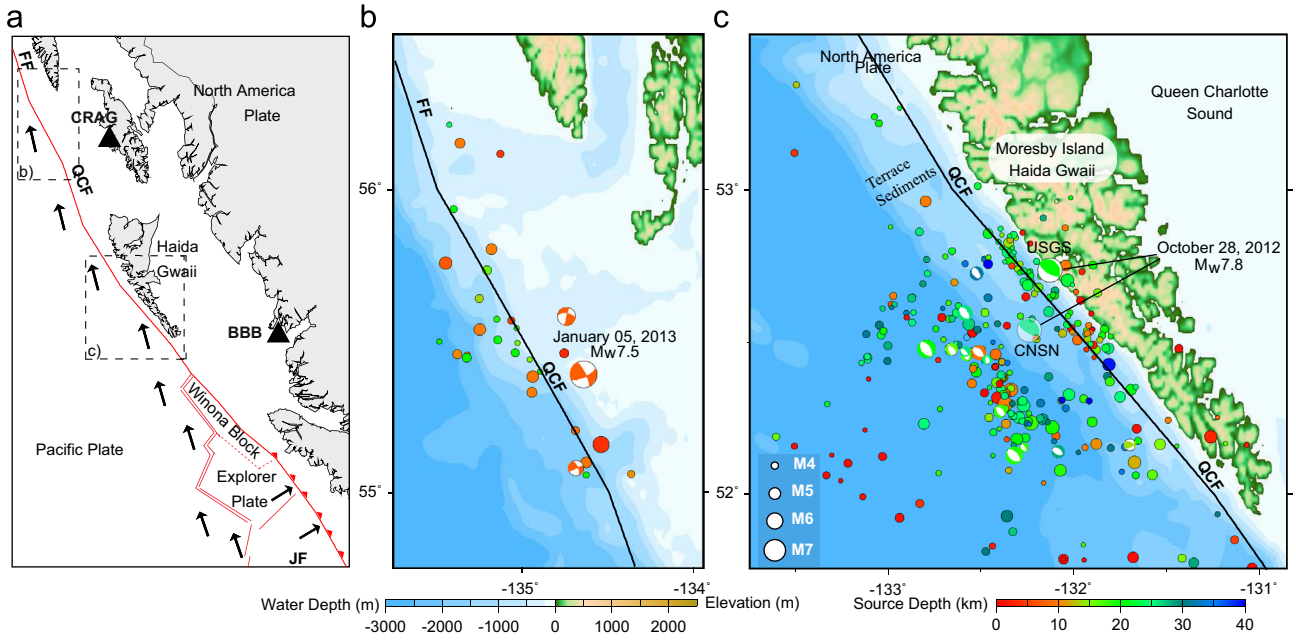


**Fig. 1.** (a) The regional plate tectonic setting of two recent large earthquakes that have struck along the plate boundary off western Canada and southeastern Alaska. The primary plate boundary is along the Queen Charlotte Fault (QCF) and the Fairweather Fault (FF), both of which are right-lateral strike–slip. The Explorer and Juan de Fuca (JF) plates underthrust North America southeast of Haida Gwaii (formerly Queen Charlotte Islands). The black vectors indicate the plate motions relative to a fixed North America for model NUVEL-1 (Argus and Gordon, 1991). The locations of regional broadband stations BBB and CRAG, used in the aftershock analysis, are indicated by black triangles. The Pacific-North America relative motion is about 50 mm/yr, with transpressional motion involving ~20% convergence along Moresby Island. (b) The January 5, 2013 ($M_w$ 7.5) strike–slip earthquake on the QCF, shown with all aftershocks with $m_b \geq 3.5$ located by the USGS NEIC and best double-couple mechanisms available from the global centroid-moment tensor (gCMT) catalog and (c) the October 28, 2012 ($M_w$ 7.8) thrust event along southern Haida Gwaii with its aftershock sequence from October 28, 2012 to November 21, 2012 with $M_L \geq 3.5$ located by the CNSN along with available best double couple solutions from the gCMT catalog for the mainshock and aftershocks plotted at the CNSN epicenters (and the USGS epicenter for the mainshock). There is a steep continental slope about 5 km seaward of the island, the base of which is the QCF (solid line), beyond which a 25–30 km wide sediment terrace extends seaward to a mild moat in the Pacific ocean floor.

1958 (Gutenberg and Richter magnitude $M_{S(G-R)}$ 7.9) St. Elias (Lituya Bay), July 30, 1972 ($M_w$ 7.6) Sitka (e.g., Schell and Ruff, 1989), and August 22, 1949 ($M_{S(G-R)}$ 8.1) Queen Charlotte events (Allen et al., 2009), the latter being the largest recorded event to strike Canada (Rogers, 1983) (historical seismicity and focal mechanisms along the QCF and FF are shown in Supplementary Fig. S1). The transpressive environment along Haida Gwaii appears to provide a logical explanation for the localized uplift of the otherwise largely submerged Wrangelia terrane emplaced along the continental margin (e.g., Yorath and Hyndman, 1983), but it has been unclear whether the relative plate motions are accommodated by underthrusting or internal plate deformation in this region. Focal mechanisms of regional events along southern Haida Gwaii indicate predominantly boundary-perpendicular compressional axes (Ristau et al., 2007), and very few modest size oblique strike–slip faulting events possibly related to the QCF in contrast to predominantly strike–slip faulting along the QCF along northern Haida Gwaii. The southern extent of the 1949 rupture is very uncertain, but that event has directivity that indicates predominant northwestward rupture from the hypocenter off of northern Haida Gwaii (Ben-Menahem, 1978).

There have been extensive studies of the Queen Charlotte margin for decades, defining the seismic, gravity, bathymetric, and geological structure of Haida Gwaii and offshore structures (e.g., Hyndman and Ellis, 1981; Yorath and Chase, 1981; Hyndman et al., 1982; Yorath and Hyndman, 1983; Horn et al., 1984). Unlike the more pronounced bends in the San Andreas system to the south, the gradual nature of the left-stepping bend in the southern QCF, the complexity of the evolving triple junction with the Explorer plate, and changes in relative motion of the Pacific and North American plate over the past 8 Myr make it difficult to evaluate the regional plate boundary structure. The current transpressive geometry has been in-place since ~4–6 Ma, a consequence of a late Miocene to early Pliocene change in absolute Pacific plate motion (e.g., Yorath and Hyndman, 1983; DeMets et al., 1987; Stock and Molnar, 1988; Hyndman and Hamilton, 1993). An accumulated convergence across the boundary of about 80–200 km, increasing northward and then tapering off, is generally expected, but the precise amount depends on the uncertain location and timing of the onset of oblique convergence; estimates as low as just tens of kilometers of convergence have been proposed (e.g., Prims et al., 1997). Accommodation of the convergence has been variously attributed to oblique subduction of a flange of the Pacific plate beneath Haida Gwaii (e.g., Hyndman and Ellis, 1981; Hyndman et al., 1982; Mackie et al., 1989; Hyndman and Hamilton, 1993; Smith et al., 2003; Bustin et al., 2004), or to internal deformation within the Pacific and/or North American plates with a vertical strike–slip plate boundary between thickened crust on either side (e.g., Horn et al., 1984; Dehler and Clowes, 1988; Rohr and Dietrich, 1992; Rohr et al., 2000; Rohr and Tryon, 2010). Significantly oblique subduction commonly leads to slip-partitioning between a thrusting interface and strike–slip faulting of an upper forearc sliver (e.g., Fitch, 1972; McCaffrey, 1992); restraining bends on strike–slip faults can be viewed as an end-member of this, with any partitioned slivers having lengths controlled by the dimensions of the bend. Along Haida Gwaii the Pacific lithosphere is quite young and warm, which could help to enable bending and underthrusting, but also limits the down-dip width of seismic coupling that might exist on the plate boundary (e.g., Smith et al., 2003).

The conflicting tectonic interpretations of the Haida Gwaii region have important implications for seismic hazard; the oblique subduction model has been the basis of asserting that megathrust events as large as $M$~8 could occur in this region (e.g., Bustin et al., 2004) while intraplate deformation models suggest that there is no likelihood of such events (Rohr et al., 2000). The ambiguity about the convergent motion placed this region as a low tsunami

risk transform boundary for the Pacific tsunami warning system and the local tsunami potential was deemed poorly understood by Leonard et al. (2010) based on extensive review of historical events and models. Under the assumption of orthogonal convergence at 8 mm/yr along a 250 km long subduction fault 32 km wide, Leonard et al. (2012) estimated a possible megathrust event size of $M_w$ 7.7 (7.5–8.0), with average recurrence interval of ~713 (266–1916) yr, with run-up on the west coast of Haida Gwaii being about 3 m. Given that the boundary parallel motion must exceed the boundary perpendicular motion by a factor of 4–5 due to the highly oblique convergence, there must either be substantial aseismic motion on the QCF or relatively frequent very large strike–slip earthquakes in the transpressional region.

On October 28, 2012, a massive, tsunamigenic thrust event ($M_w$ 7.8) with plate boundary-perpendicular convergence (Fig. 1b) definitively resolved the long-standing questions of whether the Pacific plate underthrusts Haida Gwaii (to at least some extent) and whether there is potential for large thrust earthquakes and tsunami generation in this region. We analyze the large interplate earthquakes in this region and the aftershock sequence of the October 28, 2012 event to determine the coseismic slip distribution and slip partitioning along this transpressive boundary and to assess the tsunami excitation.

## 2. Large earthquakes in 2012 and 2013

The October 28, 2012 Haida Gwaii event (03:04:08 UTC, 52.788°N, 132.101°W, 14 km depth, $m_b$=6.5, $M_S$ 7.5, USGS, http://comcat.cr.usgs.gov/earthquakes/eventpage/pde20121028030408820_14#summary) has a hypocenter beneath western Moresby Island (Fig. 1c). The USGS hypocentral estimate used observations from two stations on Haida Gwaii, and has formal uncertainties of 5.9 km (latitude) and 7.3 km (longitude) with depth uncertainty of 1.8 km. Actual uncertainties are larger, with the hypocenter estimate from the Canadian National Seismic Network (CNSN) (Fig. 1c; 52.547°N, 132.243°W, 23.2 km) being further offshore and deeper. CNSN locations are used for the aftershocks in Fig. 1c due to inclusion of arrival times from several additional local stations, but we prefer the USGS location for the mainshock due to the global coverage and more reasonable depth estimate. The spread of event locations is comparable for the USGS and CNSN catalogs, with some aftershocks clearly locating over 50 km oceanward from the QCF, and does not appear to be caused by systematic location error or bias. The CNSN locations in Fig. 1c show stronger clustering seaward of the sediments and near the QCF than the more uniformly spread USGS locations, but the overall distributions are similar.

Long-period seismic wave inversions by the USGS and global Centroid Moment Tensor project (gCMT, http://www.globalcmt.org/CMTsearch.html) for the October 28, 2012 Haida Gwaii event indicate that it was a shallow thrust event with a centroid depth in the range 11–21.5 km and seismic moment in the range 5.2–6.1 $\times 10^{20}$ N m ($M_w$ 7.7–7.8). We performed inversions of long-period W-phase signals (Fig. S2) in the frequency band 1.67–5.0 mHz for a range of source depths, finding the preferred solution shown in Fig. 2, with a centroid depth of 9.5 km, seismic moment of 6.9 $\times 10^{20}$ N m ($M_w$ 7.8), centroid time shift of 27.7 s, and a best double couple with strike 317.1°, dip 18.5°, and rake 103.3°. Inversions with centroid depths of more than 40 km give poorer fits to the W-phase data and, in particular, to later fundamental-mode surface wave arrivals. Centroid depths less than 9.5 km can still fit the W-phase data very well, but have some instability for the long-period signals (Fig. S3).

The January 5, 2013 Craig event (08:58:19 UTC, 55.394°N, 134.650°W, 7.10 km depth, $m_b$ 6.4, $M_S$ 7.8, $M_L$ 7.1, http://comcat.cr.usgs.gov/earthquakes/eventpage/pde20130105085819330_10#summary) is located northwest along the QCF (Fig. 1b), and has long-period moment tensor solutions with right-lateral strike–slip

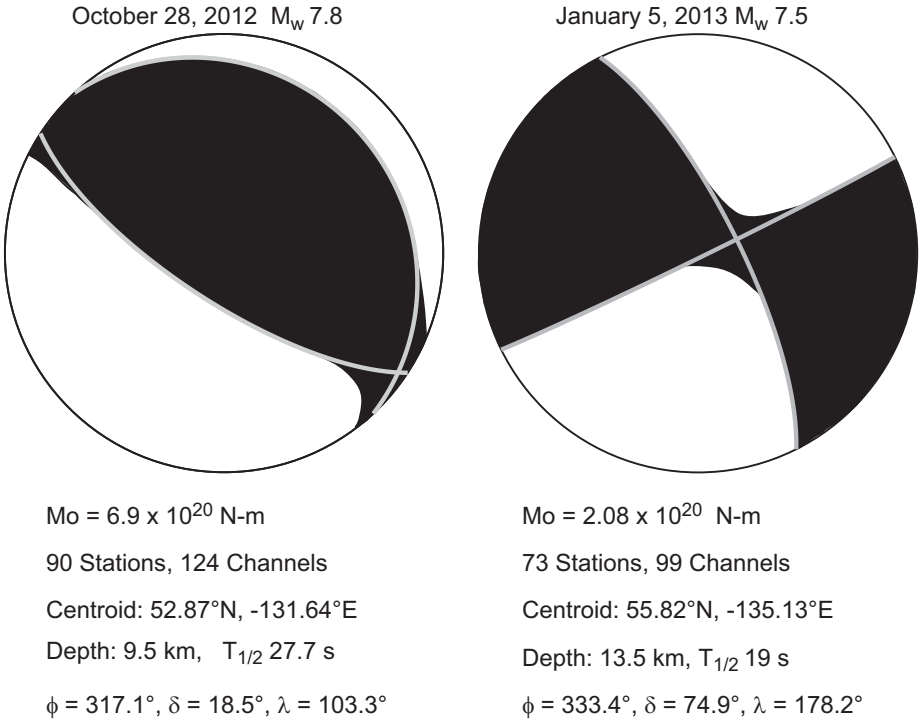


**Fig. 2.** Point-source moment tensor solutions for the two recent large events along the northeastern Pacific–North American plate boundary. These solution are for inversion of W-phase observations in the frequency band 1.67–5.0 mHz from the indicated number of stations and channels, with the seismic moment ($M_0$), centroid epicenter and depth, centroid time shift ($T_{1/2}$) and strike ($\phi$), dip ($\delta$) and rake ($\lambda$) of the best double couple being given for each case. Observed and synthetic W-phase comparisons are shown in Supplementary Fig. S2.

faulting on steeply dipping (57–78°) nodal planes parallel to the fault with seismic moment estimates in the range 2.2–2.6 × $10^{20}$ N m ($M_w$ 7.5). Location uncertainties are on the order of 5–10 km, based on comparisons of locations from the Alaska Earthquake Information Center and global determinations. There is some spread in the aftershock locations in Fig. 1b, but at least some events have mechanisms that are not consistent with QCF faulting (Fig. 1b), so the spread in locations is probably not just a result of mislocation. Our preferred W-phase inversion for this event shown in Fig. 2 has a centroid depth of 13.5 km, seismic moment of 2.1 × $10^{20}$ N m, centroid time shift of 19 s, and a best double couple with strike 333.4°, dip 74.9°, and rake 178.2°.

The 2013 event is not at all surprising, as it ruptured along the QCF in the region between the rupture zones of the 1972 Sitka and 1949 Queen Charlotte events. The 2012 event, however, was surprising to many, for it is rare to have such a large thrust event perpendicular to a predominantly strike–slip boundary, even though that possibility had been foreseen by some. The excellent fits to the distinct W-phase waveforms for the 2012 and 2013 events (see Fig. S2) confirm that the differences in mechanism are robustly resolved and that the solutions in Fig. 2 are stable characterizations of the overall seismic energy release in each event.

Finite-fault model inversions were performed for the 2012 and 2013 events using teleseismic broadband P waves and SH waves with constraints from the W-phase solutions as well as information from short-period back-projections, and for the 2012 event, also from tsunami observations. Fig. 3 summarizes the two resulting models of slip distribution from linear kinematic inversions with constant rupture velocity for model grids with strike and dip constrained by the long-period inversions. Very minor adjustment in strike (320°) for the 2012 event was made to better track the plate boundary.

For the January 5, 2013 event, 68 broadband P waves and 29 broadband SH waves were inverted, with the latter down-weighted by a factor of 0.2 to balance the amplitude information. The subfault source time functions were parameterized with 4 3-s rise-time triangles with 3-s time lags, giving 15-s subfault rupture durations. We assume a rupture expansion velocity of 2.5 km/s over a total fault length of about 120 km, finding more slip concentrated toward the northwest. The teleseismic data do not uniquely resolve the rupture velocity, and much higher velocities and longer fault extension are compatible with the data. The seismic moment estimate of 2.5 × $10^{20}$ N m is 20% larger than for the W-phase solution in Fig. 2 (both estimates have at least 20% uncertainty), with the P wave solution being somewhat less stable due to the proximity of the null axis in the down-going radiation pattern. Spatially concentrated peak slip of about 12 m is estimated. If we consider only the subfaults with well-resolved seismic moments at least 20% of the peak subfault moment, the average slip is 6.3 m (for a slip area of 960 $km^2$ and corresponding seismic moment of 2.0 × $10^{20}$ N m, with average rigidity of 33.1 GPa) and the static stress drop is 9.6 MPa, for an overall 1:5 width:length strike–slip aspect ratio. Example waveform fits are shown in Fig. S4.

For the October 28, 2012 event, 83 broadband P waves were used in the inversion, with 100 s long signals. The subfault source time functions were parameterized with 8 2-s rise-time triangles with 2-s time lags, giving 18-s subfault rupture durations. The source velocity structure was adapted from Smith et al. (2003), adding a 3 km water layer. Rupture expanded from the hypocenter at about 2.3 km/s over a total fault length of about 150 km, and most slip is up-dip from a 15.9 km deep hypocenter below western Haida Gwaii. In this case the average rupture velocity is better constrained because by iterative modeling of the tsunami observations as discussed below and has about 10% uncertainty. With an 18.5° dip, the model extends to the toe of the offshore sedimentary terrace about 40 km to the southwest, with relatively uniformly distributed shallow slip in the upper 10 km, most of which is seaward from the trace of the QCF. All of the faulting parameters have several degree uncertainties on average. We explored models

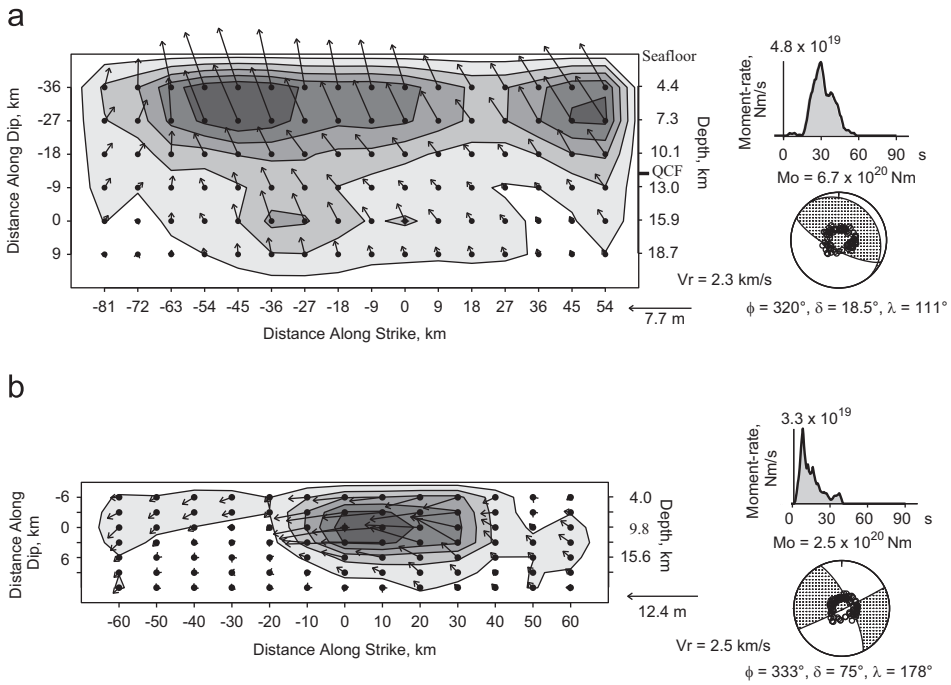


**Fig. 3.** Finite-fault slip models from teleseismic body wave inversions for (a) the October 28, 2012 Haida Gwaii and (b) the January 5, 2013 Queen Charlotte Fault earthquakes. The slip distribution on the fault plane is shown for each case with the arrows indicating average rake of each subfault and slip magnitude being contoured. Peak slip is indicated for each model, along with the rupture expansion velocity, $V_r$. The moment rate functions, seismic moments, and average focal mechanisms are shown, with the lower hemisphere equal area projections indicating the positions sampled by teleseismic P waves used in the inversions. Tsunami observations were used to constrain the solution for the Haida Gwaii event. The depth at which the QCF intersects the Haida Gwaii rupture model is indicated on the right axis of the slip model. Observed and synthetic P wave comparisons are shown in supplementary Fig. S4.

with a curved fault plane with depth-varying dip, but the data could not resolve a model more complex than the constant dip model shown here. The estimated seismic moment is $6.7 \times 10^{20}$ N m ($M_w$ 7.8), and the centroid time is 30 s, both being compatible with the W-phase inversion in Fig. 2. If we consider only the subfaults with well-resolved seismic moments at least 20% of the peak subfault moment, the average slip is 3.3 m (for a slip area of 6399 km$^2$, and corresponding seismic moment of $6.4 \times 10^{20}$ N m, with average rigidity of 30.3 GPa) and the static stress drop is 2.2 MPa, for an overall 1:4 width:length dip slip aspect ratio. Example waveform fits are shown in Fig. S4. Using the broadband teleseismic P waves we measure a radiated energy of $4.0 \times 10^{15}$ J in the passband 0.05–1.0 Hz, and by including lower frequency source spectra from the finite fault inversion moment rate function a total radiated energy of $8.8 \times 10^{15}$ J from 0.005–1.0 Hz. The USGS estimate is $5.5 \times 10^{15}$ J, but does not account for the lower frequency energy contribution. The ratio of our radiated energy to seismic moment, $Er/M_0 = 1.3 \times 10^{-5}$ (Fig. S5).

In defining the spatial extent of the fault model for the October 28, 2012 event, we incorporated general constraints from back-projections of teleseismic short-period P waves from five broadband regional networks configurations at different azimuths, using the method described by Xu et al. (2009). The networks included: (1) 72 F-Net stations in Japan; (2) 52 stations widely distributed across central Asia, east Asia, and the western Pacific Ocean; (3) 69 stations in Europe; (4) 117 stations in the eastern US, central America, and northern South America; and (5) 62 globally distributed stations. The imaged rupture characteristics were broadly similar among the different arrays and here we discuss results from the Europe array, which combined a relatively wide sampling of slowness space with high waveform coherence.

Data from broadband stations in Europe were obtained from the Orpheus data center (www.orfeus-eu.org) and vertical component traces were retained for back-projection if the first 10 s of the unfiltered P wave had an average correlation coefficient of at least 0.7 after running a multi-channel cross correlation algorithm (VanDecar and Crosson, 1990). The selected stations and corresponding traces are shown in Fig. 4a. The USGS epicenter was used in the onset alignment and the source region was gridded in increments of 0.05° from 51 to 55°N and 128 to 136°W, with depth held constant at 14 km. The imaging time began 20 s before the origin time and lasted for 120 s with increments of 1 s. Power was calculated from fourth-root beams using a 10-s tapered window.

The time integrated beam power for the European data back-projection is shown in Fig. 4b. Significant beam power exists for about 55–60 s after the nominal origin time and is located beneath

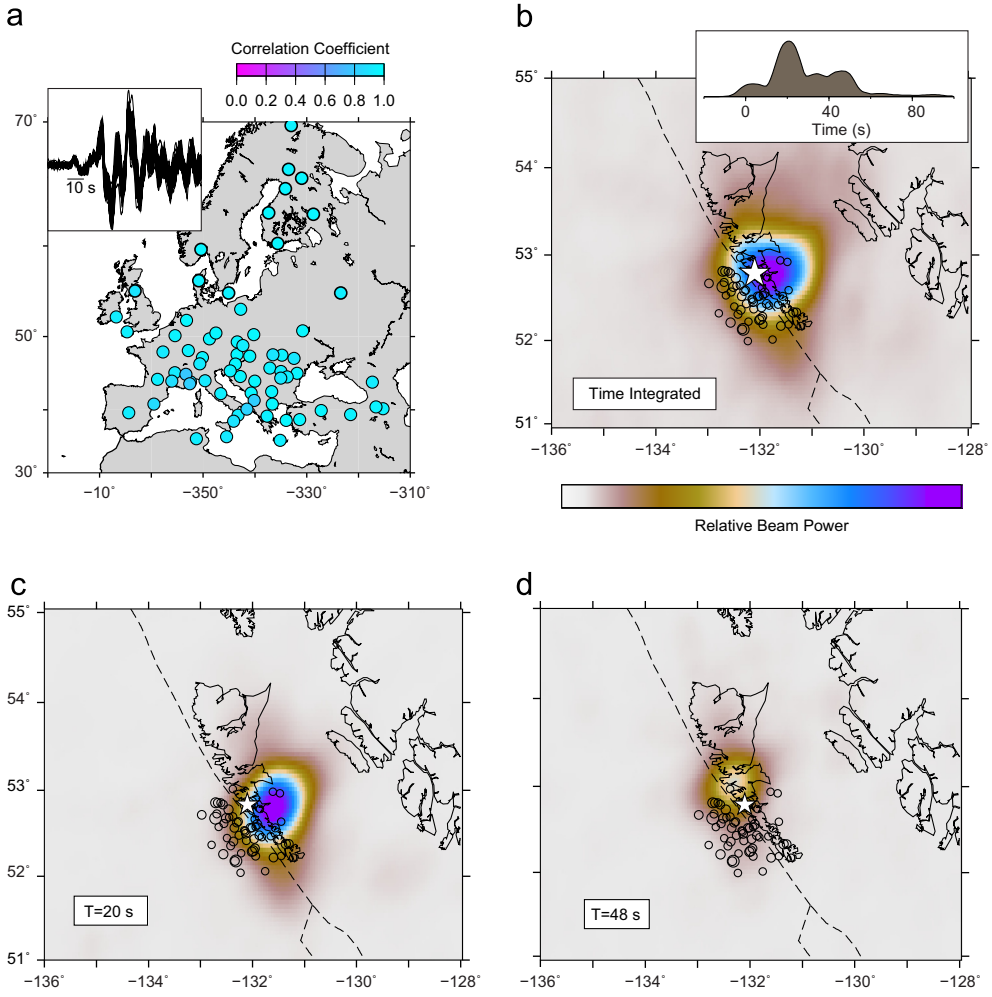


**Fig. 4.** (a) Map of station locations in Europe with superimposed broadband waveforms and correlation coefficients for each station being indicated by the color scale. (b) Map of the relative power of time-integrated coherent short-period (0.5–2.0 s) P wave radiation from the October 28, 2012 Haida Gwaii event imaged by back-projection of the signals from the 69 European stations, with power ranging from zero (white) to unity (purple). The circles are epicenters of $m_b \geq 4.0$ earthquakes located by the USGS. (c) Snapshot at 20 s into the rupture indicating the back-projected beam power showing radiation from SE of the hypocenter. (d) Snapshot at 48 s into the rupture indicating the back-projected beam power showing radiation from NW of the hypocenter. Corresponding back-projections from stations in the eastern United States are shown in Fig. S6. Animation of the full time sequence is shown in the Supplement.

Haida Gwaii landward from the QCF. The along-strike extent of significant beam power is similar to the along-strike length of early aftershocks. An animation (Animation S1) of the back-projected beam power is included in the on-line supplement and clearly indicates a bilateral component to the rupture, with the largest burst of coherent short-period radiation located southeast of the epicenter at around 20 s (Fig. 4c), and a weaker sub-event at around 48 s located northwest of the epicenter (Fig. 4d). A corresponding image of back-projections for teleseismic stations located to the southeast of the epicenter, including many Earth-scope Transportable Array stations, is shown in Fig. S6. The overall source image again lasts about 60 s and is concentrated beneath Haida Gwaii, with asymmetric bilateral rupture with stronger coherent beam power southeast of the epicenter, followed by lesser beam power to the northwest. These back-projections help to bound the total rupture dimensions and

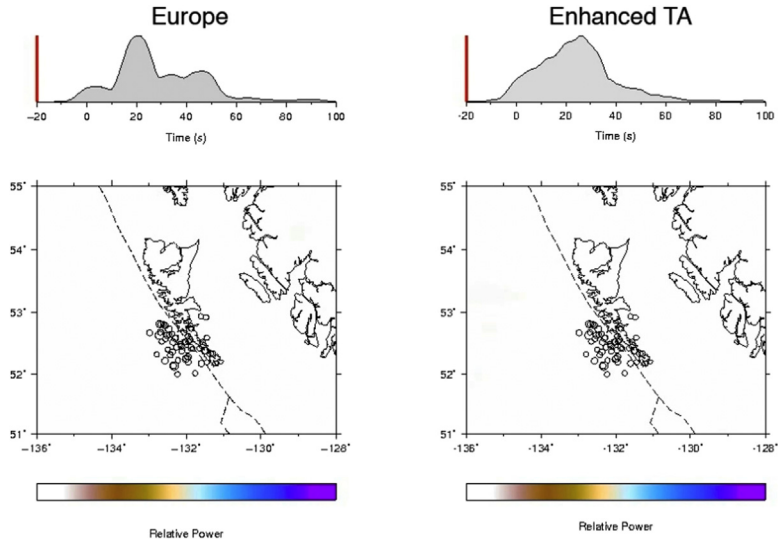


**Video S1.** A video clip is available online. Supplementary material related to this article can be found online at http://dx.doi.org/10.1016/j.epsl.2013.05.005

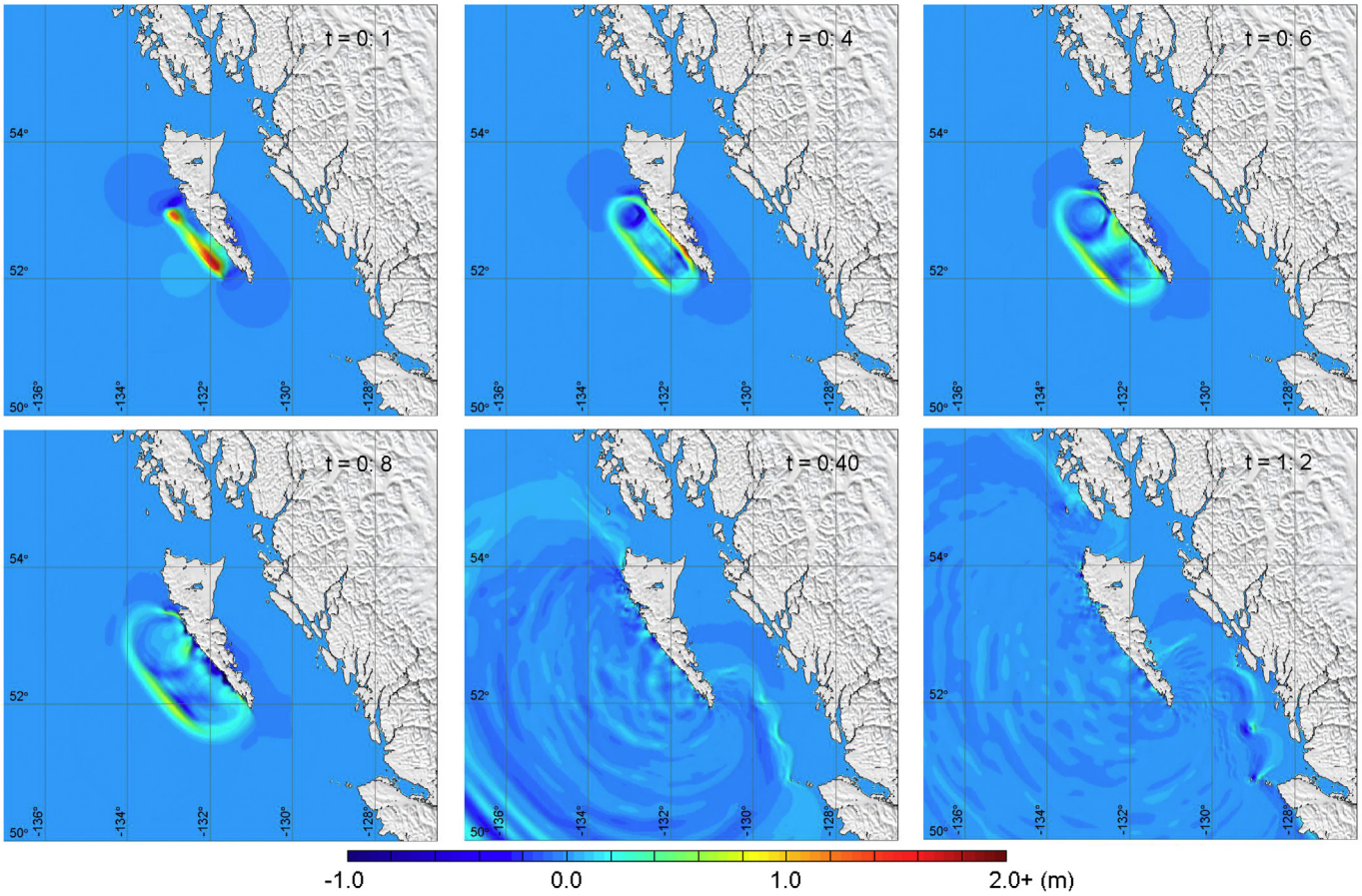


**Video S2.** A video clip is available online. Supplementary material related to this article can be found online at at http://dx.doi.org/10.1016/j.epsl.2013.05.005

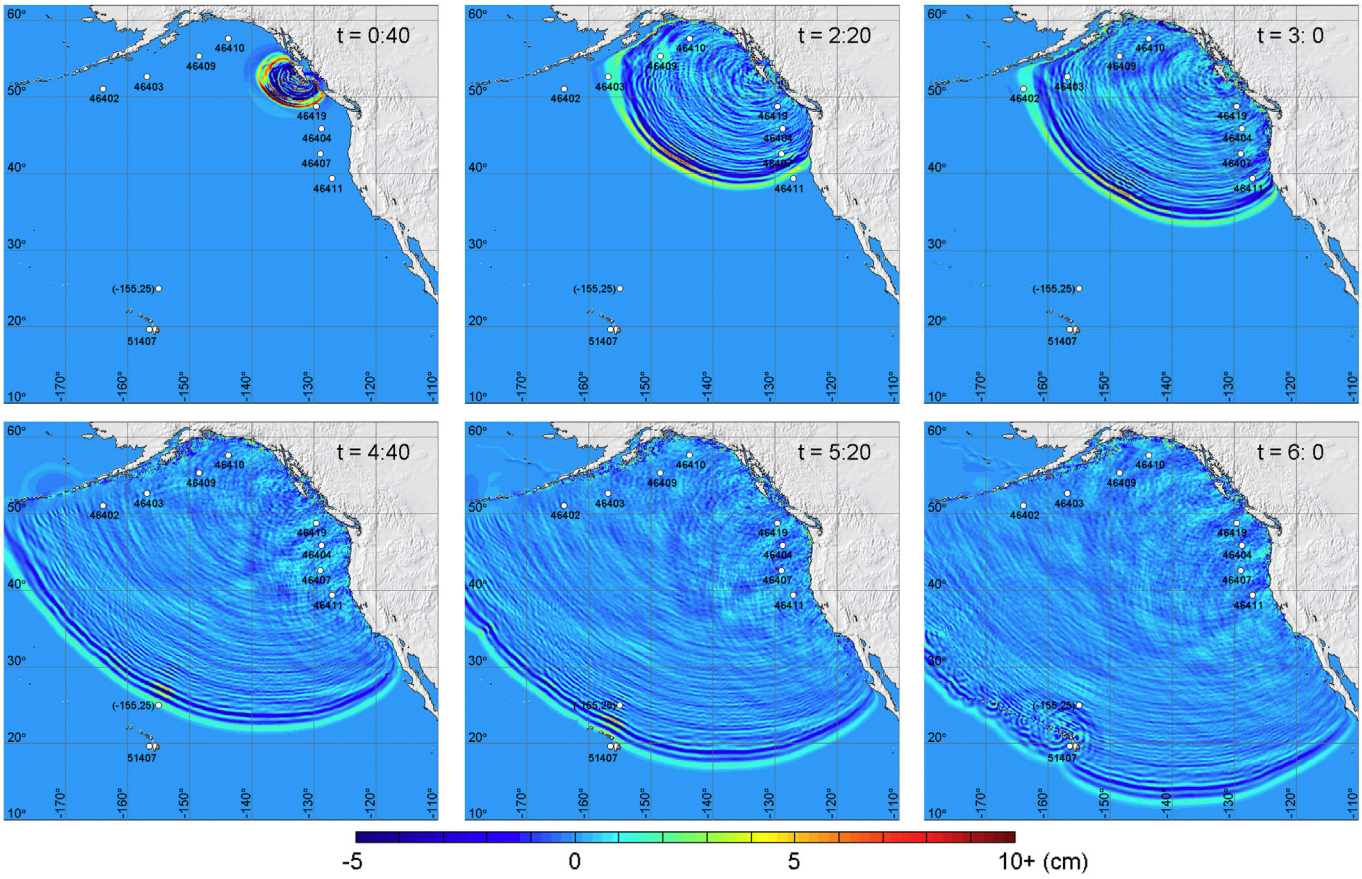


**Video S3.** A video clip is available online. Supplementary material related to this article can be found online at http://dx.doi.org/10.1016/j.epsl.2013.05.005.

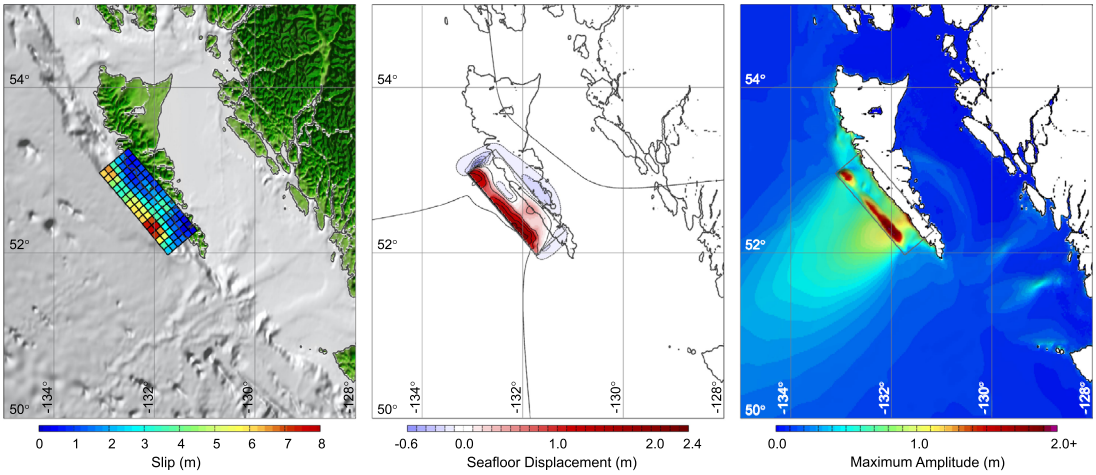


**Fig. 5.** Maps of the fault slip (left), rock surface vertical displacement (center), and maximum sea surface elevation (right) for the rupture model for the October 28, 2012 Haida Gwaii earthquake obtained by iterative modeling of teleseismic P waves and deep water tsunami recordings from DART buoys. The primary slip region is beneath the sediment terrace. The solid lines indicate 0.5-m uplift contours, and the dashed lines indicate 0.1-m subsidence contours.

rupture velocity used in the finite-fault inversion. The back-projections suggest most coherent short-period radiation occurred on the continental side of the QCF. If we use the offshore CNSN hypocenter to align the teleseismic data, there is a corresponding ocean-ward shift of the patterns, with the images locating closer to the QCF. We infer about 10–15 km uncertainty in the image locations as a result, although use of the USGS location is likely to better relate to the observed teleseismic P waves alignments. The along-dip position of the high-frequency radiation is discussed further below.

## 3. The Haida Gwaii tsunami

Tsunami observations were particularly valuable for constraining the finite-fault model for the October 28, 2012 Haida Gwaii event. Recordings by NOAA deep-water DART buoys and coastal tide gauges in Hawaii provided excellent, azimuthally well-distributed signals of the tsunami. We performed many iterations of the teleseismic P-wave inversion, adjusting model parameters such as fault dimensions, rupture velocity, dip, and hypocenter to ensure good forward modeling of the tsunami observations at the deep-water DART buoys

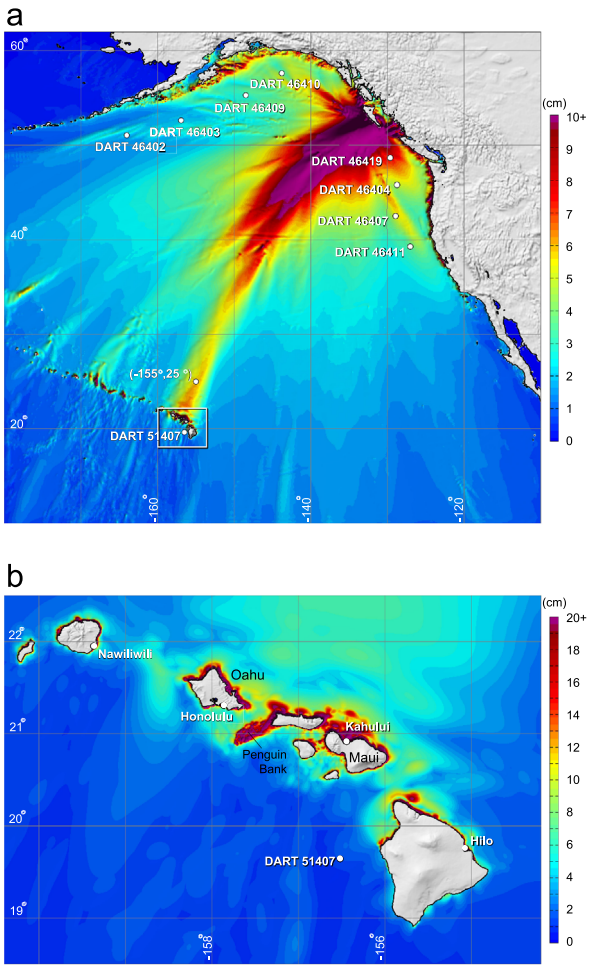


**Fig. 6.** (a) Maximum sea surface elevation computed for the model in Fig. 5 for the northeastern Pacific. White circles indicate DART and experimental water level stations, and white rectangle indicates the level-2 grid coverage for the vicinity of Hawaii expanded in (b). (b) Maximum sea surface elevation around Hawaii within the level-2 grid. White circles indicate DART and tide-gauge stations.

(Yamazaki et al., 2011b). The high-resolution multibeam and LiDAR data along the Hawaiian Islands allow modeling of the complex wave patterns at the tide gauges for independent validation of the final model. The shock-capturing dispersive wave model NEOWAVE of Yamazaki et al. (2009, 2011a) describes the tsunami from its generation by the earthquake rupture to the surges along Hawaii's coasts. The staggered finite difference model builds on the nonlinear shallow-water equations with a vertical velocity term to account for weakly-dispersive waves and a momentum conservation scheme to describe bores or hydraulic jumps. The model implements up to four levels of two-way nested-grids with 2′ (~3600 m) for tsunami propagation over the northeast Pacific, 24″ (~720 m) for wave transformation across the Hawaiian Islands, and 3″ (~90 m) around the island coasts for transition to 0.3″ (~9 m) at the tide gauge.

For a specific finite-fault inversion of the teleseismic P waves, the kinematic seafloor deformation with time-varying subfault contributions computed by the planar fault model of Okada (1985) provides the seafloor vertical displacement and velocity. NEOWAVE accounts for the time history of uplift and subsidence with its vertical velocity term in modeling of tsunami generation and kinetic energy transfer to the water. Fig. 5 shows the slip distribution and seafloor displacement for the final model in Fig. 3a as well as the maximum sea surface elevation computed at 1′ (~1800 m) resolution near the source. The rupture results in three distinct uplift patches at the epicenter and along the trench that define the near and far-field tsunami characteristics (see Supplementary Animations S2 and S3). The maximum uplift of 2.3 m at the southeast patch generates an initial surface wave of 1.9 m amplitude off Moresby Island. The sea surface elevation might have been amplified along the coast and in narrow embayments that are not well resolved by the 1' grid. Although the majority of the energy is reflected by Haida Gwaii toward the Pacific Ocean, the submarine canyons and channels southeast of Moresby Island direct a portion of the energy into Queen Charlotte Sound. Refraction over the channel banks produces distinct energy beams toward the coasts corroborating reports of localized tsunami impacts.

Fig. 6a shows the computed maximum surface elevation together with the positions of DART buoys used in the forward tsunami modeling and an hypothetical water-level station north of Hawaii. The wave field displays the azimuthal radiation pattern caused by the thrust faulting geometry and the seafloor features. Bowie Seamount, located 180 km west of Haida Gwaii, refracts and focuses the waves toward the northwest near DART 46410, while the Cobb–Eickelberg Seamount chain directs the energy toward DART 46407 and 46411 off the west coast. Constructive interference of the waves generated from the three uplift patches results in distinct energy beams radiating out to the Pacific. The seafloor uplift along the trench produces slowly attenuating waves in the normal direction that result in a major energy beam toward Hawaii. Fig. 6b plots the maximum surface elevation and locations of tide gauges in Hawaii. The north facing shores of Oahu and Maui, in the direct path of the major energy beam, experience the most significant wave activities. The oscillation extends from Maui across the insular shelf to Penguin Bank, which is known for its role in trapping of tsunami energy and resonance across the island chain (Munger and Cheung, 2008). The tide gauges, located in harbors across the islands, are exposed to a wide range of wave conditions for validation of the source model.

The observed and computed sea surface elevations and spectral amplitudes at the DART buoys, hypothetical water level station, and tide gauges are shown in Fig. 7. The results show good agreement in basic waveform, timing, amplitude, and frequency content. The buoys off Alaska and the west coast of North America in Fig. 7a recorded distinct initial waves with double or closely-spaced peaks associated with the two patches of large uplift along the trench. Matching the arrival times of the closest DART stations, which are least-affected by neglecting solid Earth elasticity and water density variation effects (e.g., Tsai et al., 2013), delimits the along-strike extent of the slip distribution more definitively than possible with the seismic waves. This, in turn, constrains the range of acceptable constant rupture velocity expansion. The short-period P-wave back-projection imaging suggests some non-uniformity in rupture expansion rate toward the southeast and northwest, but we could not resolve this with the broadband data and tsunami observations and chose to keep the rupture velocity constant. Fig. 7b shows significant transformation of the offshore tsunami signals at the experimental station across the Hawaiian Islands. Shelf, insular, and interisland resonance modes from 4 to 34 min periods modulate the incident waves to produce unique signals at the tide gauges. The surface elevation increases from 6 cm offshore to 46 cm in Nawiliwili Harbor and 74 cm in Kahului Harbor due to combined effects of shoaling and resonance. DART 51407 at 4700 m water depth 50 km west of Hawaii Island recorded the initial tsunami waves that were attenuated across the island chain, followed by short-period dispersive waves related to the width of the uplift patches along the trench.

DART 51407 and the Hawaii tide gauges recorded tsunami waves normal to the trench that exhibit strong correlation with the slip distribution in relation to the surrounding landform. The computed time series have been shifted by 2.5 min to account for delayed arrival due to simplified modeling assumptions (Tsai et al., 2013). The DART signal near Hawaii is exceptionally well-modeled with the final solution, and was not fit as well with models having slip constrained

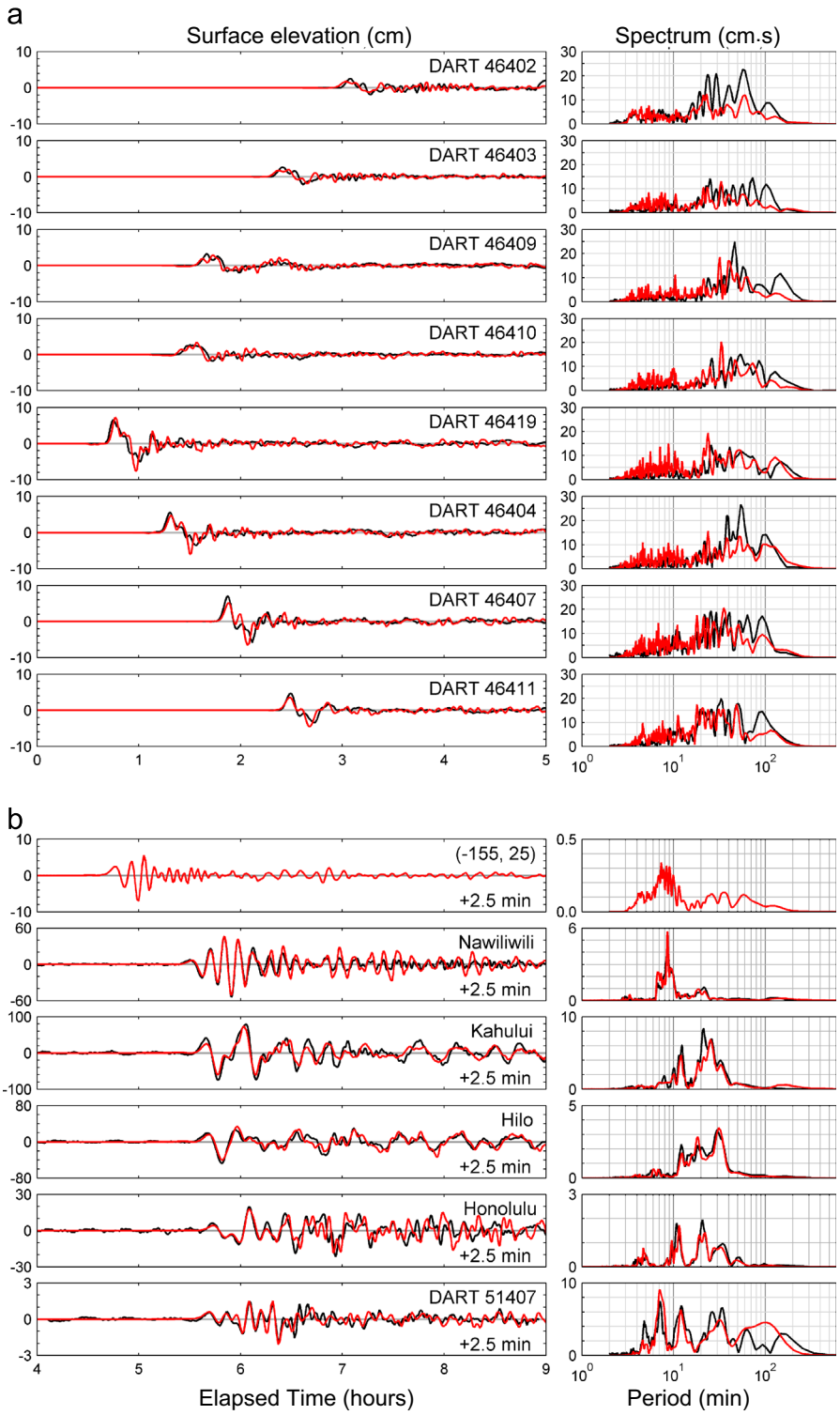


**Fig. 7.** Observed (black) and computed (red) sea surface elevation time series (left) and spectra (right) for the October 28, 2012 Haida Gwaii earthquake. The model in Fig. 5 was used as the source. (a) DART buoys along the Pacific rim at the locations in Fig. 6a. (b) Experimental water level station at (155°W, 25°N), tide gauges and DART buoy around Hawaii at the locations in Fig. 6b.

to below Haida Gwaii or extending only 20 km offshore. Since the water around Hawaii behaves as a multimodal resonator (Yamazaki et al., 2012), the good agreement obtained at the tide gauges indicates correct reproduction of the phase and frequency content of the tsunami that are directly related to the geometry and location of the uplift patches. Our final model is thus generally compatible with the broadband teleseismic P waves, short-period back-projections, and tsunami observations.

## 4. Aftershock sequence

The October 28, 2012 Haida Gwaii earthquake produced a substantial aftershock sequence with most events being located offshore beneath the sedimentary terrace or further out into the Pacific plate as much as 50 km from the QCF. We used broadband waveforms at regional stations CRAG and BBB (Fig. 1) for all events in the USGS catalog with $m_b \geq 4.0$ to evaluate the basic faulting

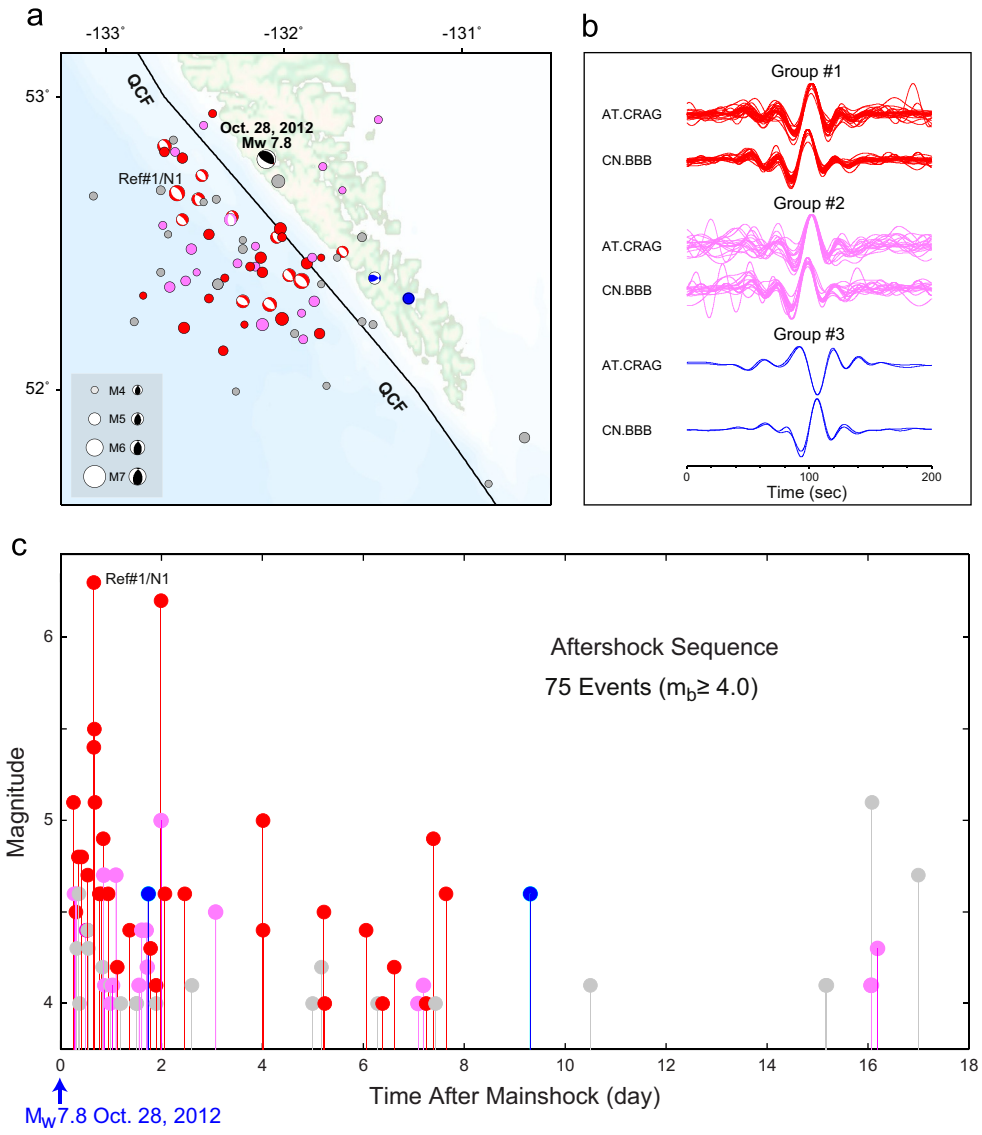


**Fig. 8.** (a) Locations of events with $m_b$≥4.0 in the October 28, 2012 Haida Gwaii event aftershock sequence from the USGS/NEIC catalog (circles), including those with gCMT solutions plotted at the NEIC locations. The black mechanism is the gCMT solution for the mainshock. The red and pink symbols (including gCMT mechanisms) indicate events with waveforms at stations BBB and CRAG (see Fig. 1) that are well-correlated with those for normal-faulting reference event #1: red indicates very high positive waveform cross-correlation coefficients, pink indicates positive moderate cross-correlation coefficients. The blue mechanisms indicate two events with high cross-correlation coefficients with one having an oblique faulting mechanism. Gray circles are for events that are not clearly identified as similar to either reference waveforms. The black line indicates the position of the Queen Charlotte Fault (QCF). (b) Superimposed waveforms for the groups of events similar to the reference normal event (Groups #1 and #2), and the oblique mechanism (Group #3). (c) Timeline for the aftershock sequence color-coded as in the map, indicating the predominance of normal faulting seaward of the QCF throughout the sequence.

categories of the aftershocks, guided by gCMT moment tensors for several of the larger events, all but one of which have normal faulting mechanisms. Cross-correlation of vertical and horizontal component regional waveforms at the two stations filtered in the passband 20–100 s allowed us to identify 31 very likely and 20 likely normal faulting events based on similarity of all components at the two nearly orthogonal stations, along with 2 oblique mechanism events and 22 unidentified events out of 75 aftershocks found to have clear signals at CRAG and BBB between October 28 and November 15, 2012. The map location of the events, the waveform clusters (Fig. S7 shows all waveform groups), and the time sequence of the aftershocks are shown in Fig. 8. Recently added gCMT solutions for smaller events confirm the preponderance of normal fault mechanisms.

It is notable that no shallow interplate thrust faulting aftershocks are included among the larger events of the aftershock sequence, and that all identified events seaward of the QCF are normal faulting events. The depths of the gCMT solutions range from 12 to 17.6 km, suggesting that these events are mostly in the Pacific plate rather than the shallow sediments. We modeled teleseismic P waves for the two largest events, finding an optimal depth of 7 km for the $M_w$ 6.4 event (N1 in Fig. 8) at 18:54:20.8 UTC on October 28, and a depth of 12 km for the $M_w$ 6.2 event (N2 in Fig. 9) at 02:49:02.3 UTC on October 30. Depth uncertainties are thus at least 5 km for the gCMT solutions. Normal faulting offsets may help to account for the rather steep average dip of the down-warping Pacific plate as it underthrusts Haida Gwaii (e.g., Hyndman et al., 1982). The two oblique mechanism aftershocks are located below land, and no purely strike–slip aftershocks along the QCF have been confirmed.

It is common to observe outer rise normal faulting aftershocks seaward of large megathrust events, and this is typically attributed to coseismic stress increments applied to bending/extensional intraplate

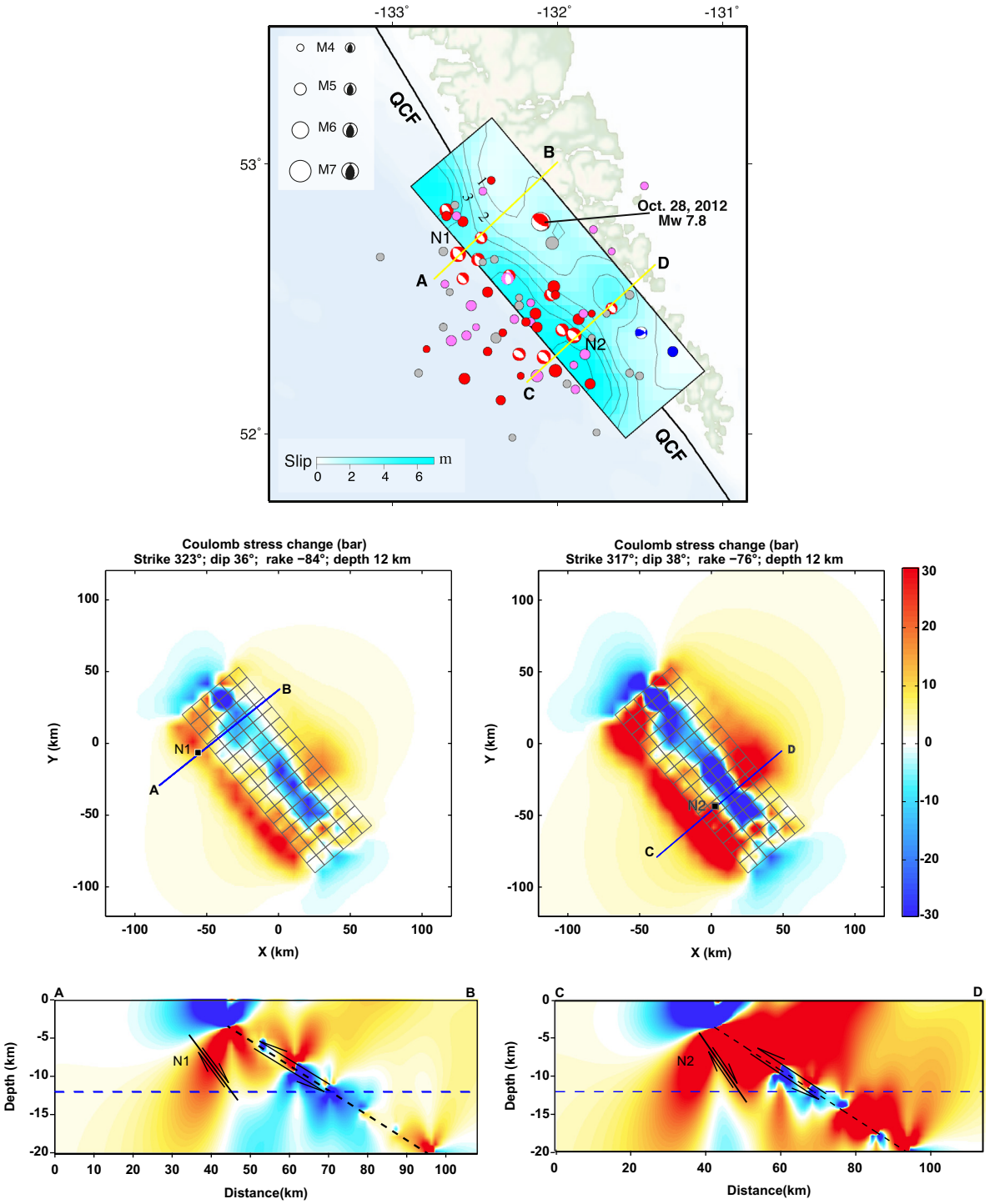


**Fig. 9.** Top, map of the slip model in Fig. 5 with aftershock locations and gCMT best-double couple solutions for the October 28, 2012 Haida Gwaii aftershock sequence. The slip model was used to compute Coulomb stress changes on two profiles, AB and CD, shown in map view and cross-section below, for target fault orientations given by the geometry of large normal faulting aftershocks N1 and N2. The color scale indicates increases (red) and decreases (blue) in driving stress (bars) on those orientations.

faults in the outer rise. The 2012 Haida Gwaii earthquake sequence certainly has this appearance, even though it involves very young lithosphere being subducted given the proximity to the triple junction with the Explorer plate. The great 1960 Chile earthquake produced extensive outer trench slope normal faulting in young lithosphere, but most regions where such sequences have been observed involve much older lithosphere. It may be that the magnitude of very shallow slip and proximity to the trench plays an important role in this phenomenon.

The Haida Gwaii sequence is notable for the lack of aftershocks further down-dip below land, and the total lack of thrusting aftershocks. This may indicate total stress drop on the thrust plane. Coulomb stress changes produced by the fault model in Fig. 3 were computed in the near-fault volume for target faulting geometries defined by northeast-dipping fault planes of the two largest normal faulting aftershocks N1 and N2 (Fig. 9), demonstrating that there is an expected favorable stress increase for normal faulting of 10–30 bar seaward of the QCF where the main aftershock sequence occurred.

The mild obliquity of the coseismic slip vectors (~21°) for the mainshock predicts mostly decrease in driving stress for right-lateral faulting on the QCF, but given the relative plate motion, a large increase in driving stress should have developed before the event, unless previous strike–slip faulting or stable sliding has been occurring on the QCF. Given that the motion of the sedimentary terrace relative to the underlying Pacific plate was mainly plate boundary perpendicular (the horizontal surface displacements are shown in Fig. S8), the sedimentary wedge is clearly moving northwestward with the Pacific plate, so it is either decoupled from the North American plate or is supporting high strains across the QCF. Boundary parallel strain was observed along Haida Gwaii prior to the event (Mazzotti et al., 2003), but was not released coseismically; it is rather hard to imagine the QCF supporting large shear strains since it truncates at a depth of about 12 km at the top of the Pacific plate and involves a sediment/hard metamorphic terrane contact boundary. Even if the local QCF has slip velocity strengthening friction and aseismic sliding, stress can be communicated across the boundary. Alternatively, the fault could be seismogenic, but currently strongly locked. There would have to have been many large strike–slip events along the boundary to balance the 3 m convergence during the 2012 event. Possibly the 1949 event ruptured this far south, though that is not resolved. The absence of coseismic strike–slip faulting or any strike–slip earthquakes give some support to the idea that the QCF is aseismic within the restraining bend and becomes seismogenic further north where it is the main Pacific/North American plate boundary. Long-term measurement of offshore deformation with seafloor bottom geodesy may be the best approach to resolving the sliding behavior of the local QCF.

## 5. Discussion

The lack of documented large strike–slip events along Moresby Island in the historic record (see Fig. S1) or in the 2012 aftershock sequence prompted us to re-examine seismic records for the August 22, 1949 ($M_{S(G-R)}$ 8.1) earthquake, as it is plausible that event could have previously accommodated some of the boundary-perpendicular or boundary-parallel motions expected for the oblique convergence direction. The 1949 earthquake has a strike–slip first-motion mechanism (e.g., Rogers, 1983), and has been estimated to have a rupture length of 265 km based on the source initial phase of Love waves recorded at Pasadena (Ben-Menahem, 1978), and 490 km based on aftershocks (Bostwick, 1984). For a 265 km long rupture and a rupture velocity of 3.5 km/s, as used by Ben-Menahem, a source duration of about 76 s (38 s half-duration) is estimated for the 1949 event, compared to half-durations of 28 and 19 s (Fig. 2) for the 2012 and 2013 events, respectively. We used records from the large 2012 Haida Gwaii and 2013 QCF events from modern instruments to compare to the handful of historic seismograms available for the 1949 event, including Wiechert seismograms from Göttingen, short-period seismograms from Strasbourg, Wood–Anderson torsion seismograms from Pasadena, Mainka seismograms from Fukuoka, and Omori seismograms from Mizusawa.

Comparison of the Pasadena Benioff strain seismogram spectrum published by Ben-Menahem (1978) with predictions for the 2012 and 2013 events shows that the 200 s period spectral amplitude for 1949 is about 4.5 times larger ($\Delta M_w = 0.4$) relative

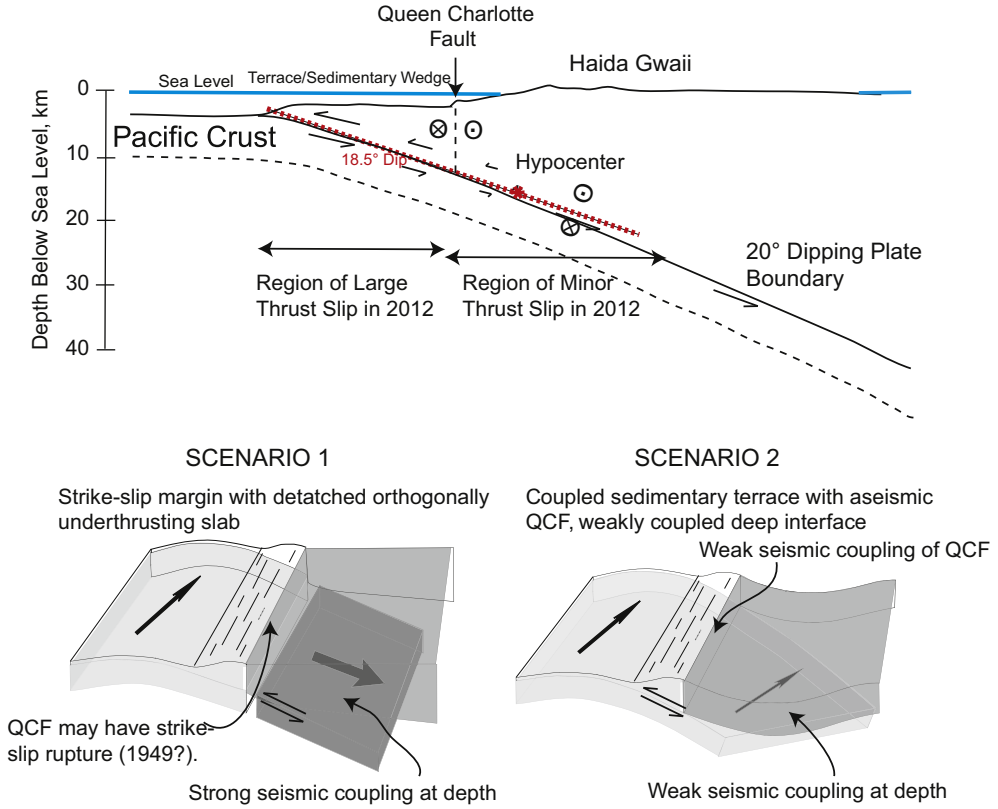


**Fig. 10.** Schematic scenario for the October 28, 2012 Haida Gwaii slip partitioning. A simplified cross-section perpendicular to the plate boundary is shown at the top, with no vertical exaggeration. The Pacific plate is underthrust below Haida Gwaii with the Queen Charlotte Fault (QCF) extending down about 10 km to the top of the Pacific plate. The rupture initiated just under the coast for the slip model with an 18.5° dip indicating large, purely dip-slip offset beneath the offshore terrace and little seismic radiation from oblique plate motion under the island. This rules out Scenario 1, which postulates a seismically coupled detached slab beneath the island, and favors Scenario 2, with oblique underthrusting with little deep seismic coupling between the Pacific plate and Haida Gwaii, but boundary-perpendicular strain accumulation and release in the sedimentary wedge, which has either low seismic coupling across the QCF or intermittent large strike–slip faulting that has not been observed historically.

to either event. For the 2012 event we measure $M_{S(G-R)}=7.2$ (corresponding to $M_S=7.4$, similar to the USGS value), which underpredicts the 1949 value if increased by ~0.4 units. We measure $M_{S(G-R)}=7.6$ for the 2013 event (corresponding to $M_S=7.8$, which is the same as the USGS value), and this almost matches the 1949 $M_{S(G-R)}$ if we add 0.4 units. Assuming similar strike–slip geometry relative to the 2013 event, we estimate $M_w$~7.9 for the 1949 event. Comparison of the relative amplitudes of P, S and surface wave phases on three-component Göttingen Wiechert records with simulations based on 2012 and 2013 records from broadband station BFO indicates that a strike–slip orientation is more reasonable than a purely thrust event for 1949, and the same is found for Wood–Anderson recordings at PAS, short-period records at Strasbourg, and Mainka records at Fukuoka. While we cannot reliably bound the southern rupture terminus for 1949, the characterization of that event as predominantly strike–slip with a rupture length of about 265 km and $M_{S(G-R)}$ 8.1, $M_w$ 7.9 appears valid.

The October 28, 2012 Haida Gwaii event seems to have nucleated below the western coast of Moresby Island, but most slip occurred offshore, below the sedimentary wedge, with purely thrusting motion, requiring dramatic slip partitioning in this transpressive boundary. Geodetic measurements of deformation on Haida Gwaii indicate upper plate strain generally in the relative plate motion direction (e.g., Mazzotti et al., 2003; Hippchen, 2011), so tectonic stress does appear to be communicated across the plate boundary. However, this is not reflected in the recent seismic activity, which has not involved significant plate-boundary parallel faulting or oblique thrusting. If we consider the simplified geometry of the convergent zone and our faulting model, as depicted in Fig. 10, we can evaluate slip-partitioning scenarios in the new light of the occurrence of the $M_w$ 7.8 boundary-perpendicular thrust event.

There is a few kilometer uncertainty in the precise location of the hypocenter, but it is certainly not far from the QCF. Our fault model predicts an intersection of the QCF with the underthrust plate at a depth of about 12 km, compatible with the scenario of Bustin et al. (2007). There is minor, poorly resolved slip on the deeper portion of our slip model that would involve direct contact between the Pacific and North American plates and a means for communicating the transpressive tectonic stress that gave rise to the pre-mainshock geodetic motions. The eastward extent of underthrust material is not resolved by the 2012 faulting and in Fig. 10 it is extrapolated based on the observation of the 20°-dipping reflector beneath eastern Haida Gwaii imaged by Bustin et al. (2007).

The notion of a detached underthrust flange of the Pacific plate that is subducting perpendicular to the boundary (Fig. 10: Scenario 1) is not consistent with the finite-faulting model and tsunamigenesis of the October 28, 2012 event. Such a model would still require large slip on the QCF to accommodate the boundary-parallel motion. If there is weak seismic coupling (or very short underthrust extent) between a continuous underthrust Pacific plate and the North American plate (Fig. 10: Scenario 2), the almost pure thrusting displacement in the 2012 event must occur between the sedimentary wedge and the Pacific crust, with the wedge having translated with the Pacific plate along the QCF during prior strike–slip earthquakes, with little resistance, or with a large shear strain accumulation. The QCF appears to act as a back-stop that forces the terrace to accumulate compressional strain perpendicular to the margin as the Pacific plate and terrace move toward the north-northwest. If the QCF is offsetting aseismically, this region is an extreme case of slip-partitioning in which the predominant strike–slip component is locally aseismic and the minor convergent component generates the main seismogenic strain accumulation. In such a scenario, there may be no significant strike–slip faulting along Moresby Island (microseismicity like that observed by Hyndman and Ellis (1981) could be present, of course). Given the required slip-partitioning, the only alternative is to have the narrow, sedimentary/hard rock contact zone of the QCF build up and release strains from several times more total displacement than occurred on the thrust interface. Possibly the 1949 event could have ruptured into this area, but there is no clear evidence of that having happened. The lack of historical strike–slip faulting on the local QCF segment, absence of strike–slip energy release in this event, and absence of strike–slip aftershocks, tend to support the possibility of aseismic deformation (slip velocity strengthening) on the QCF, but this is not resolved.

The coherent short period energy imaged by the back-projection for the 2012 mainshock locates downdip of the offshore large slip region, suggesting some energy release on the deeper plate contact, but this may involve minor seismic moment along the down-dip edge of the rupture, as has been found for deep bursts of short-period radiation during recent great megathrust events (e.g., Lay et al., 2012). It is reasonable that a narrow, coupled region on the Pacific/continental crust boundary below the Haida Gwaii coast helps to lock up the system and transmits tectonic stress from the relative plate motions to the upper plate, but when it fails with minor oblique slip the predominant coseismic slip up-dip is arc-normal with such large radiation that it overwhelms any oblique slip energy release at depth. The eastward extent to which the Pacific plate penetrates is not resolved by the seismic energy release in 2012, but the large size of the thrust event indicates that underthrusting does play a major role in the transpressional deformation. It seems plausible that the 2012 event is about the largest size thrust event that can be supported by the convergent system here, and the region is now well-calibrated for future early tsunami warning procedures.

## Acknowledgments

We thank Roy Hyndman for comments on the manuscript. This work made use of GMT, SAC, Coulomb 3.0 and Matlab software. The IRIS DMS data center was used to access the seismic data from Global Seismic Network and Federation of Digital Seismic Network stations. DART buoy data were obtained from the NOAA National Data Buoy Center. W.H.K. Lee participated in the analysis of historic seismic records for the 1949 event. This work was supported by NSF grants EAR-1245717 (T.L.).

## Appendix A. Supplementary materials

Supplementary data associated with this article can be found in the online version at http://dx.doi.org/10.1016/j.epsl.2013.05.005.

## References

Allen, T.I., Marano, K.D., Earle, P.S., Wald, D.J., 2009. PAGER-CAT: a composite earthquake catalog for calibrating global fatality models. Seismol. Res. Lett. 80, 57–62, http://dx.doi.org/10.1785/gssrl.80.1.57.

Argus, D., Gordon, R., 1991. No-net-rotation model of current plate velocities incorporating plate motion model NUVEL-1. Geophys. Res. Lett., 18, http://dx.doi.org/10.1029/91GL01532.

Ben-Menahem, A., 1978. Source mechanism of the 1906 San Francisco earthquake. Phys. Earth Planet. Inter. 17, 163–181.

Bostwick, T.K., 1984. A Re-examination of the August 22, 1949 Queen Charlotte Earthquake (M.S. thesis). Department of Geophysics and Astronomy, The University of British Columbia, 126 pp.

Bustin, A.M., Hyndman, R.D., Cassidy, J. Mazzotti, S., 2004. Strain partitioning of oblique convergence: initiation of subduction on the Queen Charlotte Margin? EOS Trans. AGU 85, Jt. Assem. Suppl. Abstract T31C-02.

Bustin, A.M.M., Hyndman, R.D., Kao, H., Cassidy, J.F., 2007. Evidence for underthrusting beneath the Queen Charlotte margin, British Columbia, from teleseismic receiver function analysis. Geophys. J. Int. 171, 1198–1211, http://dx.doi.org/10.1111/j.1365-246.X.2007.03583.x.

Dehler, S.A., Clowes, R.M., 1988. The Queen Charlotte Islands refraction project, Part I, The Queen Charlotte Fault Zone. Can. J. Earth Sci. 25, 1857–1870.
DeMets, C., Gordon, R.G., Stein, S., Argus, D.F., 1987. A revised estimate of Pacific-North America motion and implications for western North America plate boundary zone tectonics. Geophys. Res. Lett. 14, 911–914.
Fitch, T.J., 1972. Plate convergence, transcurrent faults and internal deformation adjacent to southeast Asia and the western Pacific. J. Geophys. Res. 77, 4432–4460.
Hippchen, S., 2011. Slip Partitioning, Crustal Tectonics and Deformation of the Queen Charlotte Margin and Northern Vancouver Island (Ph.D. thesis). School of Earth and Ocean Sciences, University of Victoria, 204 pp.
Horn, J.R., Clowes, R.M., Ellis, R.M., Bird, D.N., 1984. The seismic structure across an active oceanic/continental transform fault zone. J. Geophys. Res. 89, 2107–3120.
Hyndman, R.D., Ellis, R.M., 1981. Queen Charlotte fault zone: microearthquakes from a temporary array of land stations and ocean bottom seismographs Can. J. Earth Sci. 18, 776–788.
Hyndman, R.D., Hamilton, T.S., 1993. Queen Charlotte area Cenozoic tectonics and volcanism and their association with relative plate motions along the north-eastern Pacific margin. J. Geophys. Res. 98, 14,257–14,277.
Hyndman, R.D., Lewis, T.J., Wright, J.A., Burgess, M., Chapman, D.S., Yamano, M., 1982. Queen Charlotte fault zone: heat flow measurements. Can. J. Earth Sci. 19, 1657–1669.
Lay, T., Kanamori, H., Ammon, C.J., Koper, K.D., Hutko, A.R., Ye, L., Yue, H., Rushing, T.M., 2012. Depth-varying rupture properties of subduction zone megathrust faults. J. Geophys. Res. 117, B04311, http://dx.doi.org/10.1029/2011JB009133.
Leonard, L.J., Rogers, G.C., Hyndman, R.D., 2010. Annotated bibliography of references relevant to tsunami hazard in Canada. Geological Survey of Canada Open File 6552, 269 pp.
Leonard, L.J., Rogers, G.C., Mazzotti, S., 2012. A preliminary tsunami hazard assessment of the Canadian coastline. Geological Survey of Canada Open File 7201, 126 pp.
Mackie, D.J., Clowes, R.M., Dehler, S.A., Ellis, R.M., Morel-A-L'Huissier, P., 1989. The queen charlotte islands refraction project. Part II. Structural model for transition from Pacific plate to North American plate. Can. J. Earth Sci. 26, 1713–1725.
Mazzotti, S., Hyndman, R.D., Flück, P, Smith, A.J., Schmidt, M., 2003. Distribution of the Pacific/North America motion in the Queen Charlotte Islands–S. Alaska plate boundary zone. Geophys. Res. Lett. 30 (14), 1762, http://dx.doi.org/10.1029/2003GL017586.
McCaffrey, R., 1992. Oblique plate convergence, slip vectors, and forearc deformation. J. Geophys. Res. 97, 8905–8915.
Munger, S., Cheung, K.F., 2008. Resonance in Hawaii waters from the 2006 Kuril Islands Tsunami. Geophys. Res. Lett. 35 (7), L07605, http://dx.doi.org/10.1029/2007GL032843.
Okada, Y., 1985. Surface deformation due to shear and tensile faults in a half space. Bull. Seismol. Soc. Am. 75 (4), 1135–1154.
Prims, J, Furlong, K.P., Rohr, K.M.M., Govers, R., 1997. Lithospheric structure along the Queen Charlotte margin in western Canada: constraints from flexural modeling. Geo-Mar. Lett. 17, 94–99.
Ristau, J., Rogers, G.C., Cassidy, J.F., 2007. Stress in western Canada from regional moment tensor analysis. Can. J. Earth Sci. 44, 127–148.
Rogers, G.C., 1983. Seismotectonics of British Columbia (Ph.D. thesis). Department of Geophysics and Astronomy, The University of British Columbia, 257 pp.
Rohr, K.M.M., Dietrich, J.R., 1992. Strike slip tectonics and development of the Tertiary Queen Charlotte basin, offshore western Canada: evidence from seismic reflection data. Basin Res. 4, 1–20, http://dx.doi.org/10.1111/j.1365-2117.1992.tb00039.x.
Rohr, K.M.M., Tryon, A.J., 2010. Pacific-North America plate boundary reorganization in response to a change in relative plate motion: offshore Canada. Geochem. Geophys. Geosyst. 11, Q06007, http://dx.doi.org/10.1029/2009GC003019.
Rohr, K.M.M., Scheidhauer, M., Trehu, A.M., 2000. Transpression between two warm mafic plates: the Queen Charlotte Fault revisited. J. Geophys. Res. 105, 847–8172.
Schell, M.M., Ruff, L.J., 1989. Rupture of a seismic gap in southeastern Alaska: the 1972 Sitka earthquake ($M_S$ 7.6). Phys. Earth Planet. Inter. 54, 241–257.
Smith, A.J., Hyndman, R.D., Cassidy, J.F., Wang, K., 2003. Structure, seismicity, and thermal regime of the Queen Charlotte Transform Margin. J. Geophys. Res. 108 (B11), 2539, http://dx.doi.org/10.1029/2002JB002247.
Stock, J.M., Molnar, P., 1988. Uncertainties and implication of the Late Cretaceous and Tertiary position of North America relative to the Farallon, Kula, and Pacific plates. Tectonics 8, 99–115.
Tsai, V., Ampuero, J.-P., Kanamori, H., Stevenson, D.J., 2013. Estimating the effect of earth elasticity and variable water density on tsunami speeds. Geophys. Res. Lett. 40, 492–496, http://dx.doi.org/10.1002//grl.50147.
VanDecar, J.C., Crosson, R.S., 1990. Determination of teleseismic relative phase arrival times using multi-channel cross-correlation and least squares. Bull. Seismol. Soc. Am 80, 150–169.
Xu, Y., Koper, K.D., Sufri, O., Zhu, L., Hutko, A.R., 2009. Rupture imaging of the $M_w$ 7.9 12 May 2008 Wenchuan earthquake from back projection of teleseismic P waves. Geochem. Geophys. Geosyst. 10, Q04006, http://dx.doi.org/10.1029/2008GC002335.
Yamazaki, Y., Kowalik, Z., Cheung, K.F., 2009. Depth-integrated, non-hydrostatic model for wave breaking and run-up. Int. J. Numer. Methods Fluids 61 (5), 473–497.
Yamazaki, Y., Cheung, K.F., Kowalik, Z., 2011a. Depth-integrated, non-hydrostatic model with grid nesting for tsunami generation, propagation, and run-up. Int. J. Numer. Methods Fluids 67 (12), 2081–2107.
Yamazaki, Y., Lay, T., Cheung, K.F., Yue, H., Kanamori, H., 2011b. Modeling near-field tsunami observations to improve finite-fault slip models for the 11 March 2011 Tohoku earthquake. Geophys. Res. Lett. 38, L00G15, http://dx.doi.org/10.1029/2011GL049130.
Yamazaki, Y., Cheung, K.F., Pawlak, G., Lay, T., 2012. Surges along the Honolulu coast from the 2010 Tohoku tsunami. Geophys. Res. Lett. 39, L096064, http://dx.doi.org/10.1029/2012GL047508.
Yorath, C.J., Chase, R.L., 1981. Tectonic history of the Queen Charlotte Islands and adjacent areas-A model. Can. J. Earth Sci. 18, 1717–1739.
Yorath, C.J., Hyndman, R.D., 1983. Subsidence and thermal history of Queen Charlotte Basin. Can. J. Earth Sci. 20, 135–159.

# The October 28, 2012 $M_w$ 7.8 Haida Gwaii underthrusting earthquake and tsunami: Slip partitioning along the Queen Charlotte Fault transpressional plate boundary

Thorne Lay [a], Lingling Ye [a], Hiroo Kanamori [b], Yoshiki Yamazaki [c], Kwok Fai Cheung [c], Kevin Kwong [d], Keith D. Koper [d]

[a] *Department of Earth and Planetary Sciences, University of California Santa Cruz, Santa Cruz, CA 95064, USA*
[b] *Seismological Laboratory, California Institute of Technology, Pasadena, CA 91125, USA*
[c] *Department of Ocean and Resources Engineering, University of Hawai'i, Honolulu, HI 96822, USA*
[d] *Department of Geology and Geophysics, University of Utah, Salt Lake City, UT 84112, USA*

---

**Supplementary Information Figures S1-S8, Animations S1-S3**

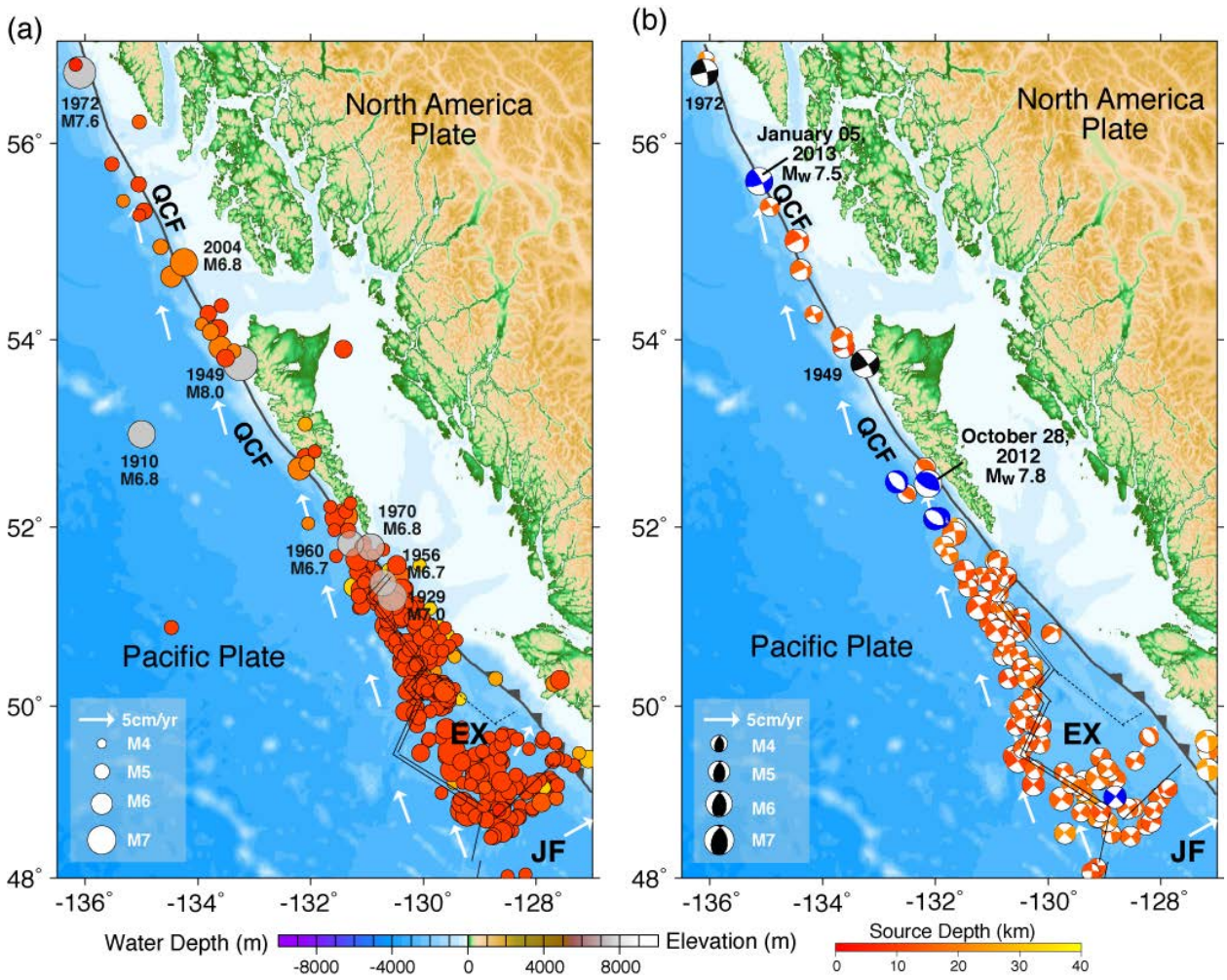


**Fig. S1**. Regional historical seismicity maps: (a) USGS/NEIC catalog earthquake locations for $m_b \geq 4.5$ (circle size is proportional to magnitude and color indicates source depth) from 1973 up to just before the October 28, 2012 event, along with $M \geq 6.5$ events (gray circles ) from 1900 to 1973 from PAGER-CAT (Allen et al., 2009); and (b) the best double-couple of moment tensor solutions from the Global CMT catalog from 1976-2012, plotted at the centroid locations. Arrows indicate Pacific plate and Juan de Fuca plate motion direction and rate relative to the North America Plate computed using model NUVEL-1 (Argus and Gordon, 1991).

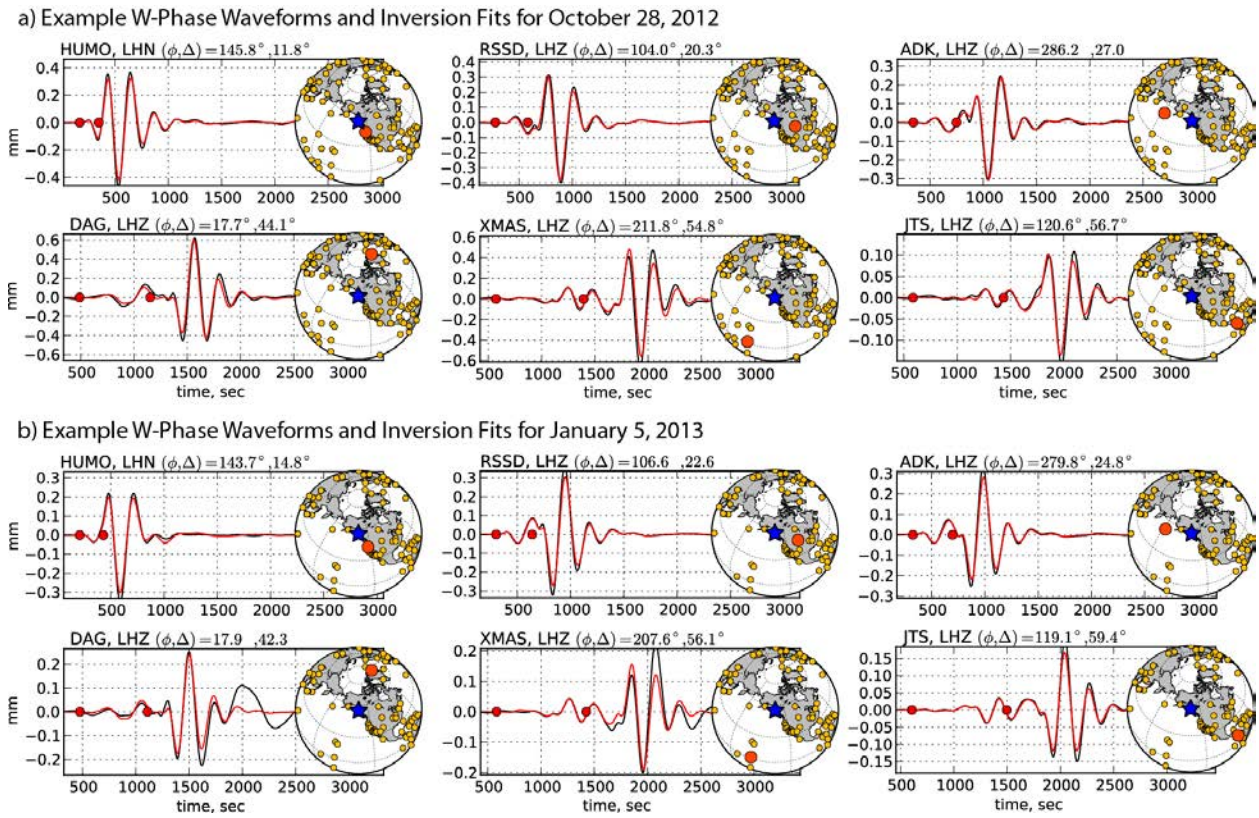


**Fig. S2.** Example W-phase observations (black traces) and computed waveforms (red) for the point-source moment tensors in Figure 2 for a) October 28, 2012 Haida Gwaii and b) January 5, 2013 Queen Charlotte Fault events. The data are from global seismic network stations with ground displacement filtered in the frequency band 0.00167-0.005 Hz. The W-phase signal used in the inversions is the waveform interval between the red dots. The large amplitude signals after the W-phase are fundamental mode surface waves and the waveform comparisons are predictions for those signals. The maps indicate the position of the station (red dot) among the total set of stations (gold dots) used in the corresponding W-phase inversion. Station DAG for the 2013 event has some non-linear response following the surface wave, well outside the W-phase window. Comparable waveform matches are found for all of the stations indicated in the maps.

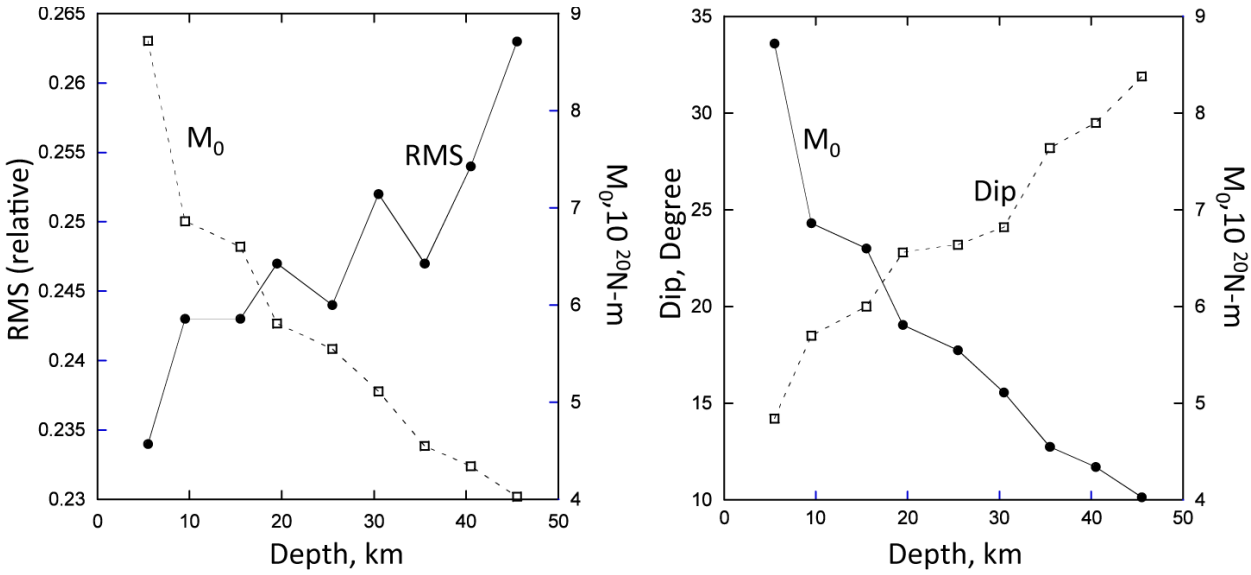


**Fig. S3**. Results of W-phase inversions for different source depths for the October 28, 2012 Haida Gwaii event. On the left, the relative waveform RMS residual is shown as a function of centroid depth, along with the seismic moment ($M_0$) estimate for each source depth. On the right the dip for the best-double couple mechanism for each moment tensor is shown for various centroid depths. As the dip decreases the seismic moment increases.

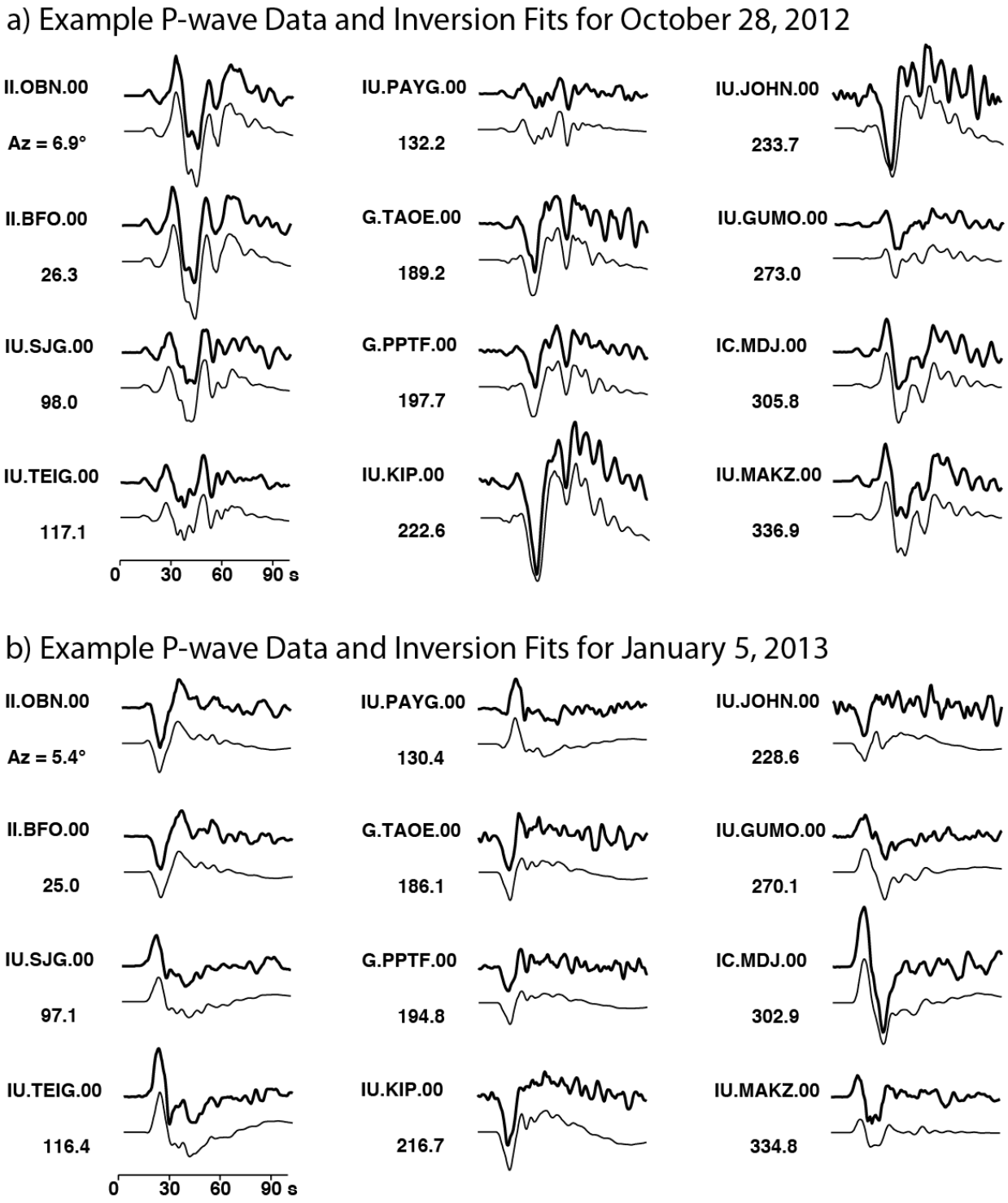


**Fig. S4.** Comparison of observed (bold lines) and modeled (thin lines) broadband P waves for the **a)** October 28, 2012 Haida Gwaii and **b)** January 5, 2013 Queen Charlotte Fault earthquakes. In both cases the models shown in Figure 3 are used for the computations. The signals are broadband ground displacements in the passband 0.005-0.9 Hz. Comparable waveform matches are found for all of the stations used in the inversions.

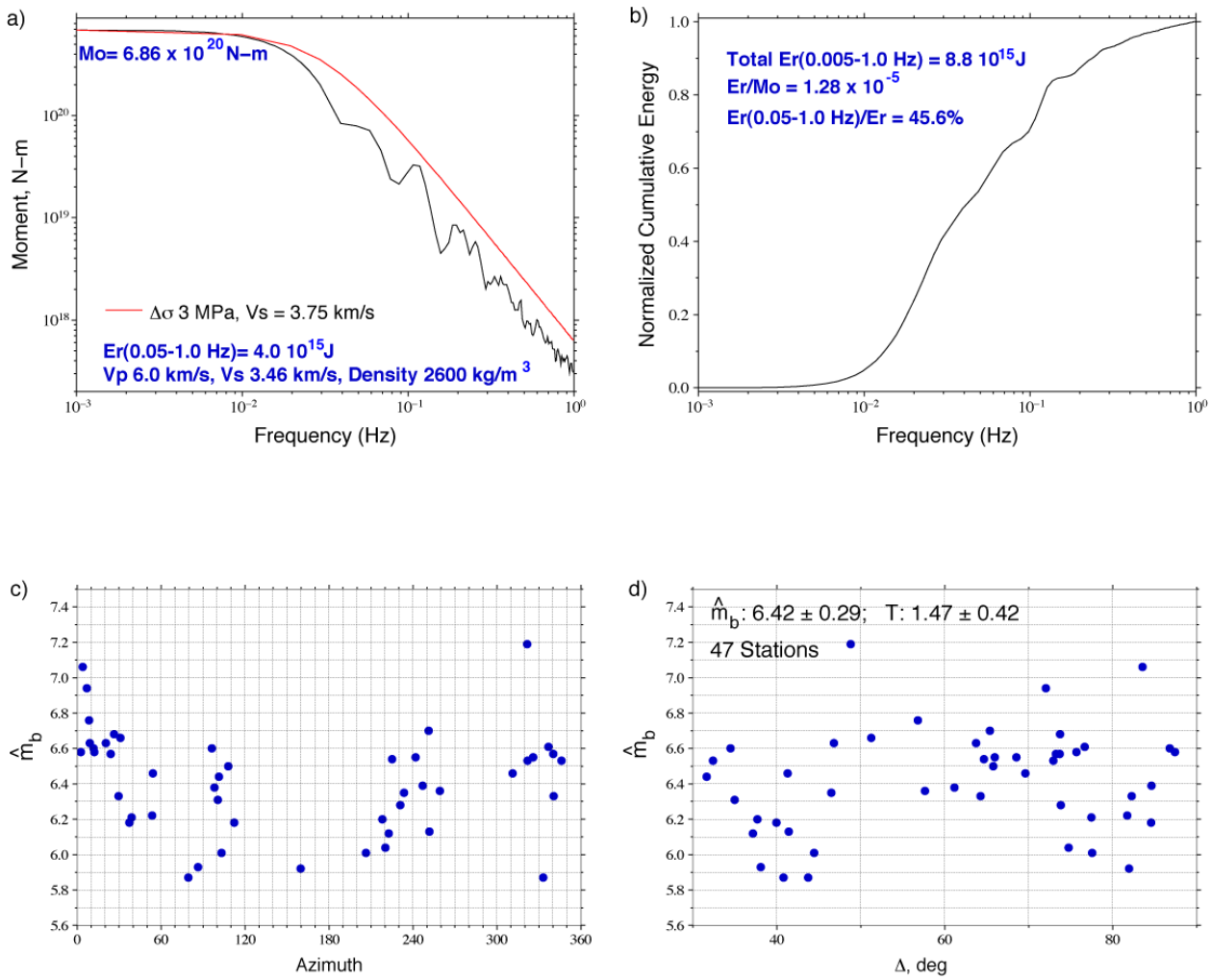


**Fig. S5**. a) Source spectrum for the October 28, 2012 Haida Gwaii $M_w$ 7.8 event earthquake obtained from combining the spectrum of the finite-source model from P wave inversion (Figure 3) for frequencies below 0.05 Hz with a averaged spectra of broadband P waves for frequencies from 0.05 to 1.0 Hz. The radiated energy from the latter passband is 4.0 x $10^{15}$ J. A reference ω-squared source spectrum with a stress drop parameter of 3 MPa is shown for comparison. b) Cumulative energy as a function of frequency over the passband from 0.005 to 1.0 Hz, with a total energy, Er, of 8.8 x $10^{15}$ J. The ratio of $Er/M_0$ = 1.28 x $10^{-5}$. c) Azimuthal pattern of short-period $\hat{m}_b$ measurements. d) Distance distribution of short-period $\hat{m}_b$ measurements, along with the average value of 6.42 for 47 stations.

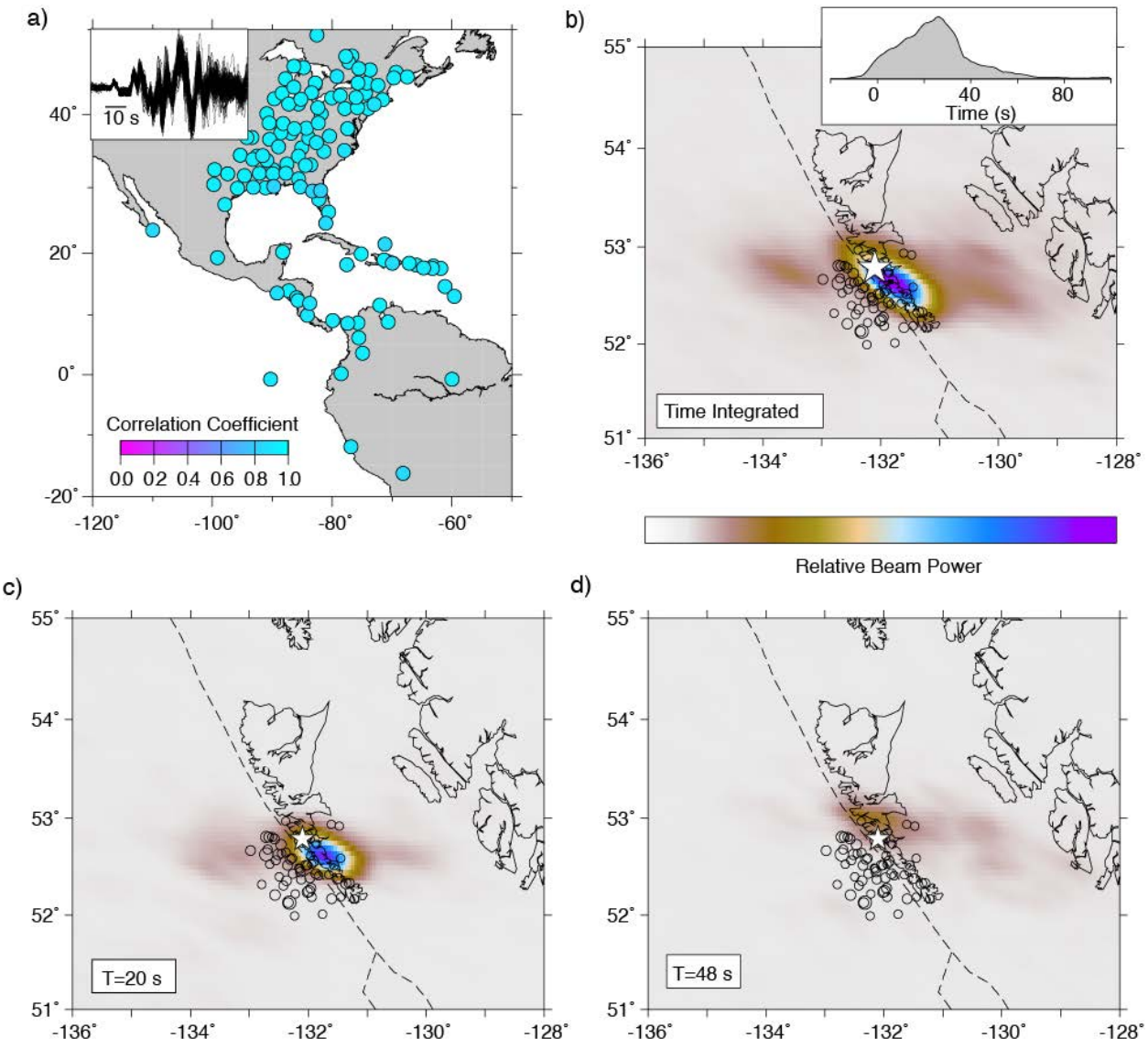


**Fig. S6. a)** Map of station locations toward the southeast from the 2012 Haida Gwaii earthquake with superimposed broadband waveforms and correlation coefficients for each station being indicated by the color scale. **b)** Map of the relative power of time-integrated coherent short-period (0.5-2.0 s) P wave radiation from the October 28, 2012 Haida Gwaii event imaged by back-projection of the signals from the 117 stations in **a)**, with power ranging from zero (white) to unity (purple). **c)** Snapshot at 20 s into the rupture indicating the back-projected beam power showing radiation from SE of the hypocenter. **d)** Snapshot at 48 s into the rupture indicating the back-projected beam power showing radiation from NW of the hypocenter. Animations of the full time sequence is shown in Animation S1.

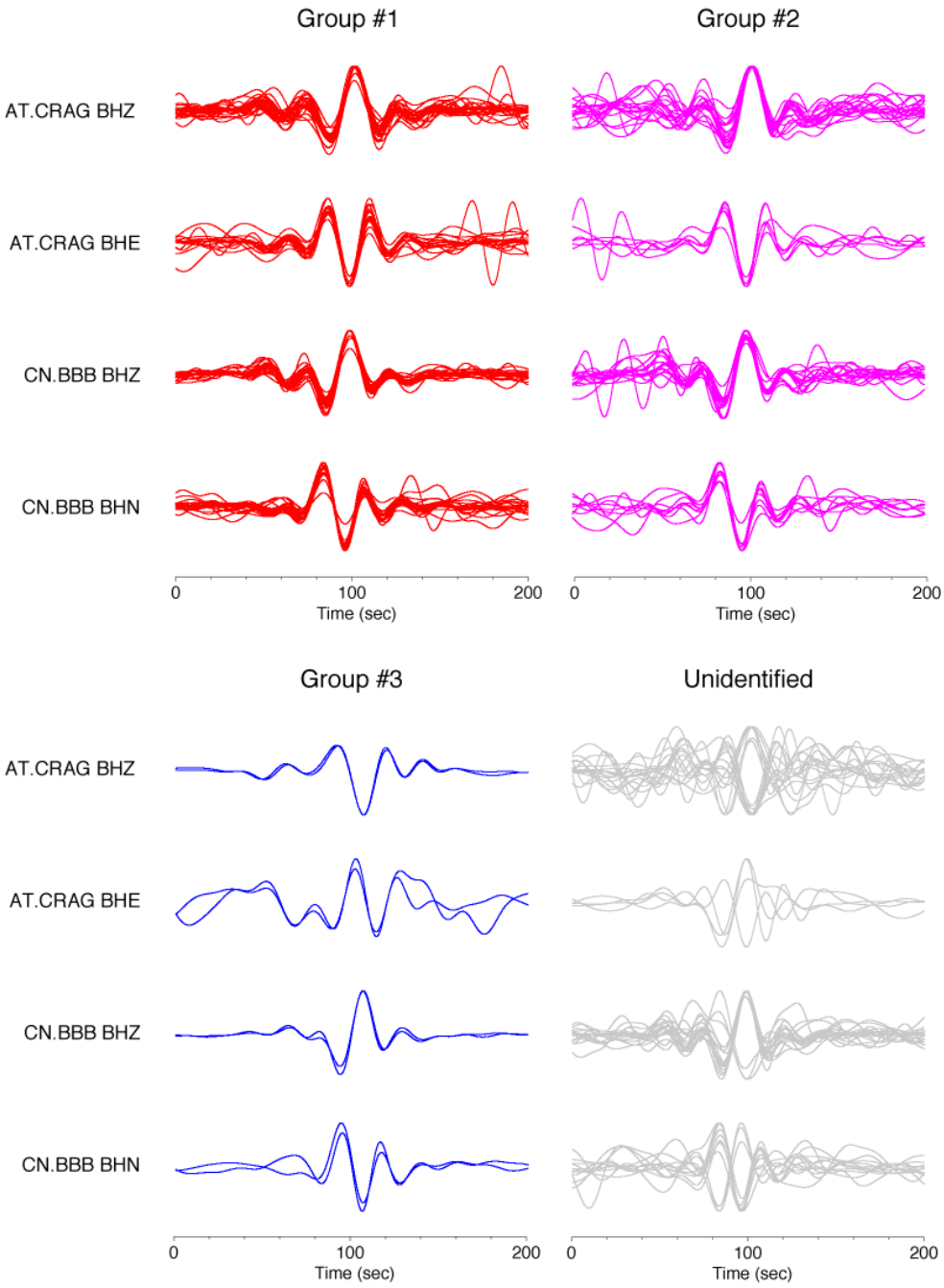


**Fig. S7**. Superposition of amplitude-scaled waveforms for 20-100 s period signals from aftershocks of the October 28, 2012 Haida Gwaii earthquake sorted into 4 groups. Groups #1 and #2 are probably all normal faulting events given the high correlation with waveforms for Reference event 1, which has a GCMT normal faulting solution. High correlations of vertical and horizontal components at stations CRAG and BBB are found for these groups with all positive correlation coefficients in the range 0.6-1.0 for assignment to Group #1 and positive correlations greater than 0.5 for assignment to Group #2. Group #3 involves oblique slip events with distinct waveforms. Unidentified events have waveforms that may have high noise or mixed sign correlations between stations and components. Most may be normal faulting, but a few are clearly distinct.

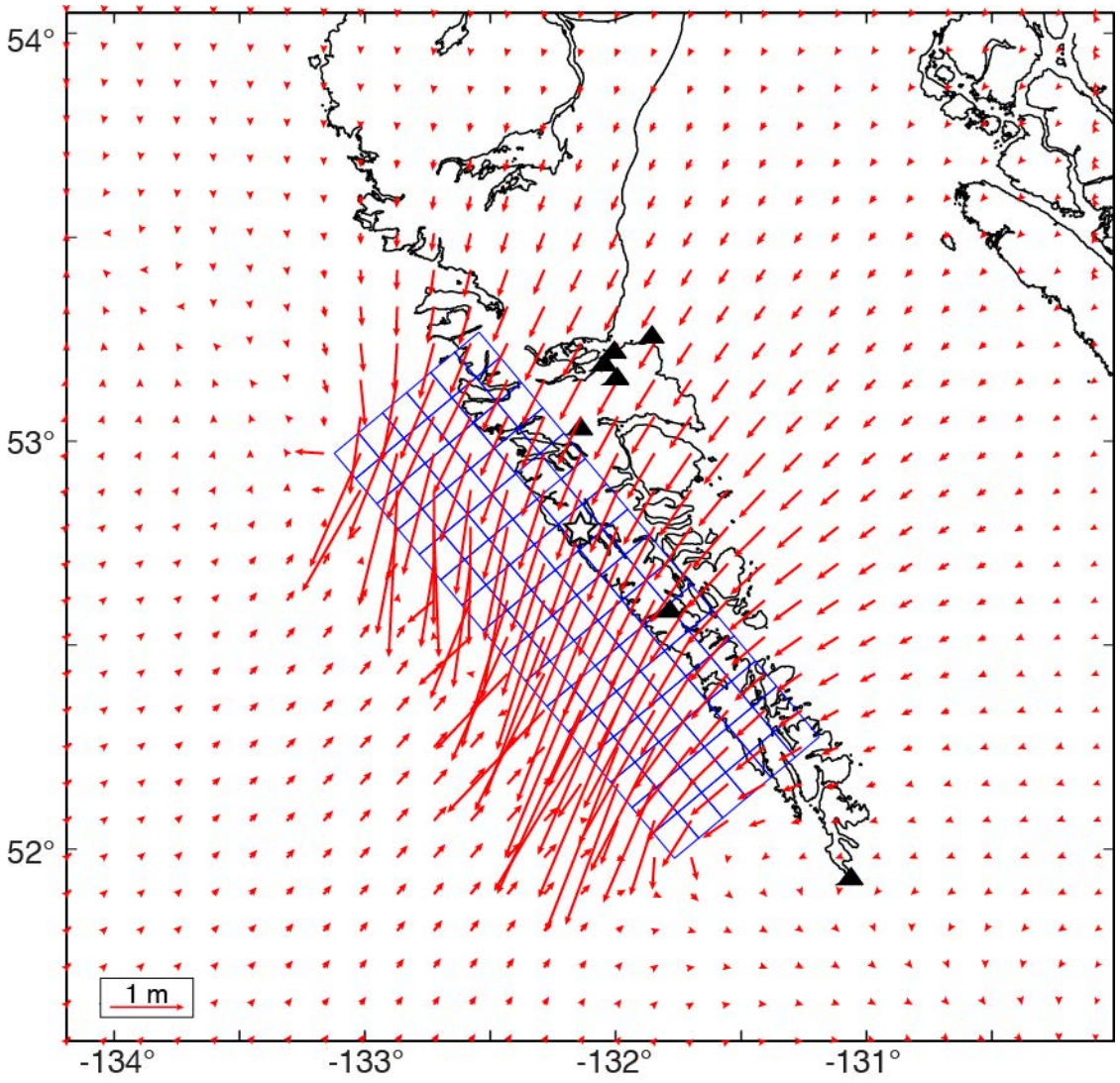


**Fig. S8**. Horizontal surface displacements predicted for the preferred fault model for the October 28, 2012 Haida Gwaii earthquake. The star indicates the USGS epicentral location on the surface projection of the 18.5° dipping model grid (rectangle). The triangles indicate locations of campaign and high-rate GPS stations. Data from those stations are not yet distributed.

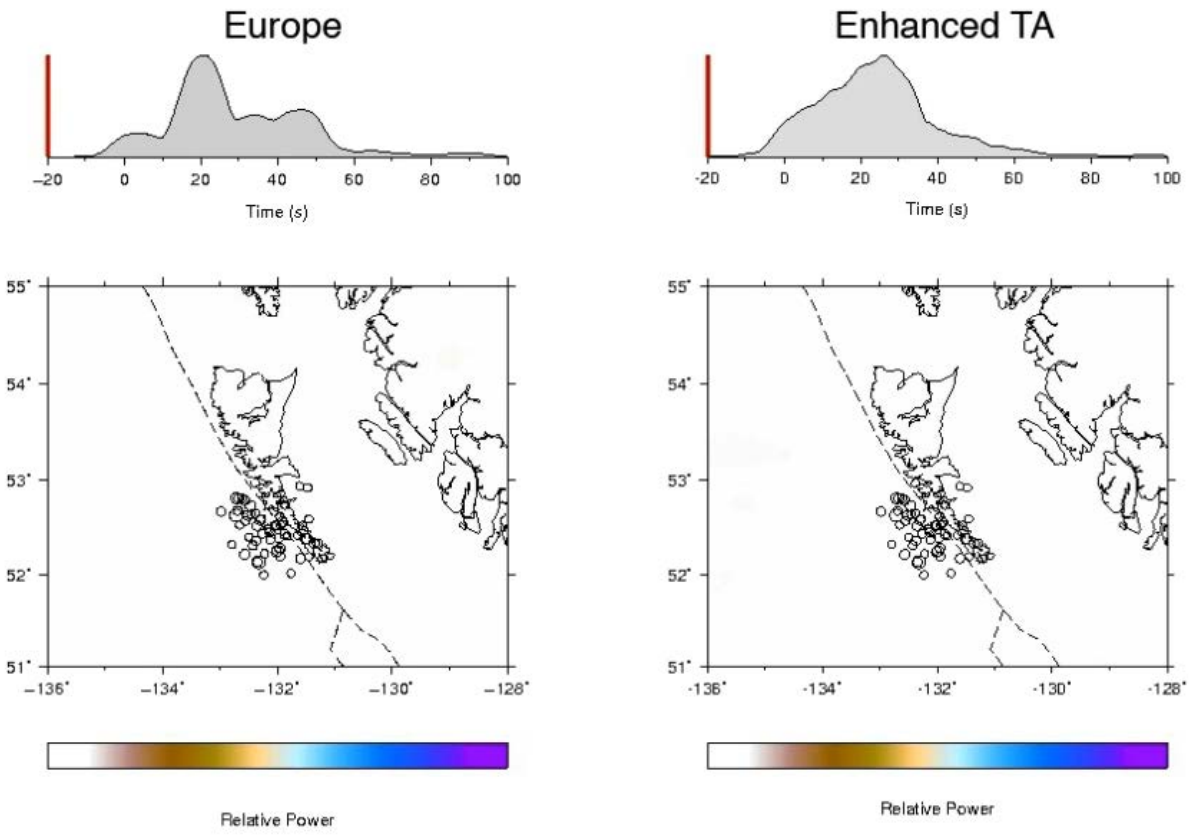


**Animation S1.** Time-sequence animations of the back-projections of the teleseismic short-period P waves recorded in Europe (Figure 4) and at azimuths to the southeast (Figure S4) for the October 28, 2012 Haida Gwaii earthquake. The relative power of the beam at each position around the source region, normalized the peak beam power for the entire time sequence is shown by the color scale, ranging from zero (white) to unity (purple).

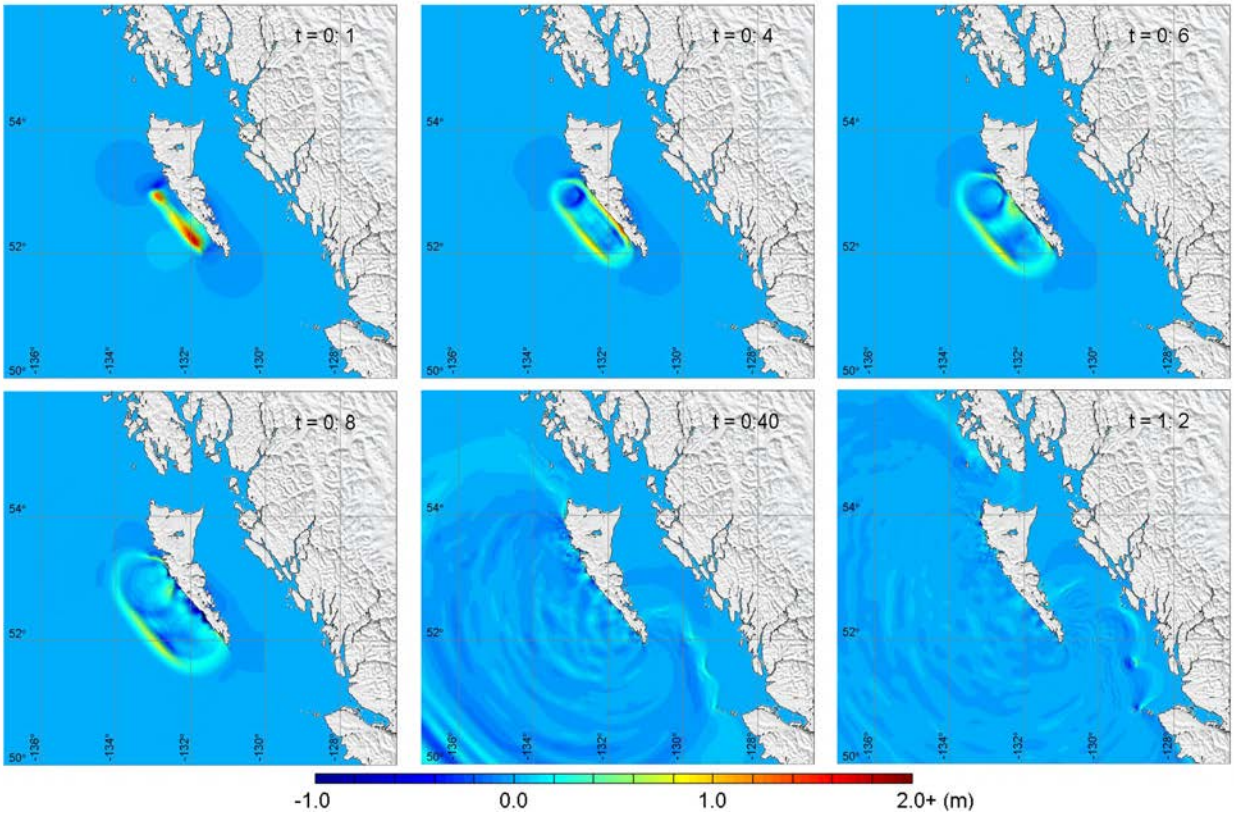


**Animation S2.** Time evolution of the computed sea surface showing tsunami generation and propagation near the rupture area.

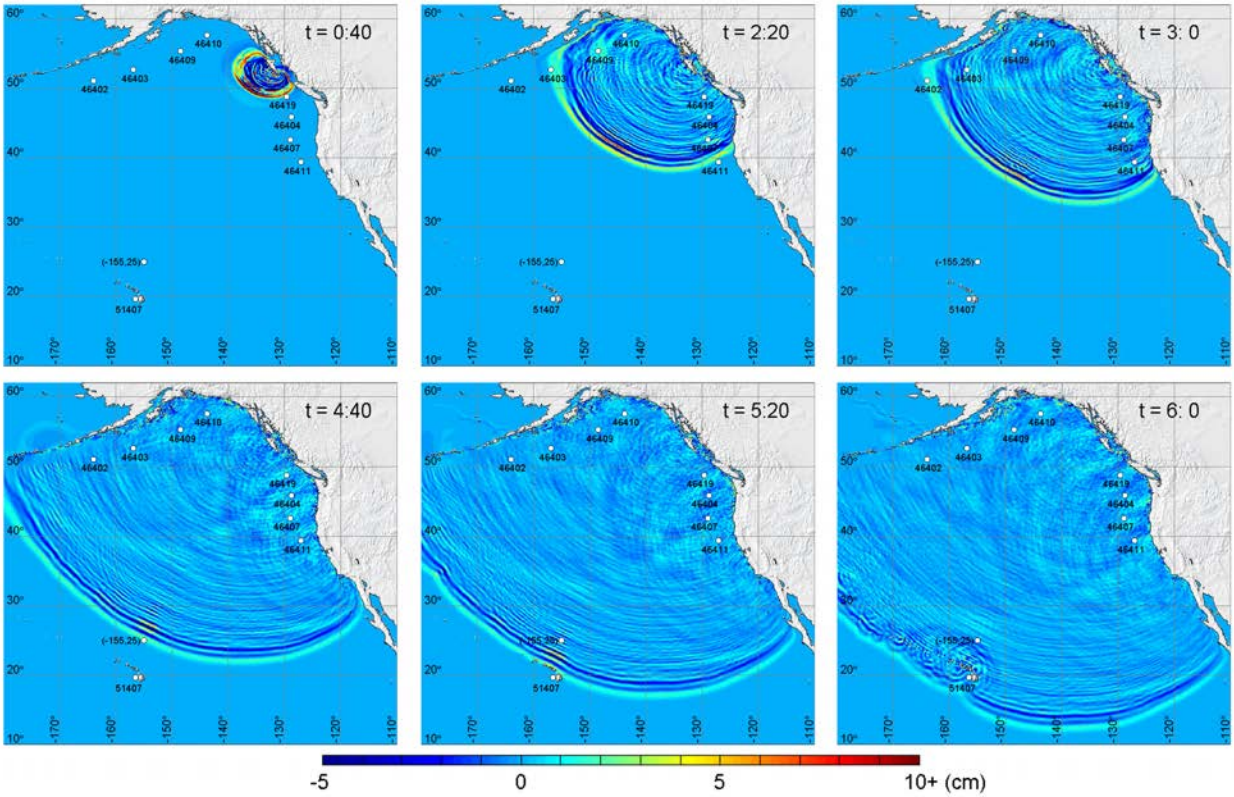


**Animation S3.** Time evolution of the computed sea surface showing tsunami propagation over northeast Pacific. White circles indicate water level stations.